

1 **A Multiscale Spatio-Temporal Big Data Fusion Algorithm from Point to**
2 **Satellite Footprint Scales**

3 **Dhruva Kathuria¹, Binayak P. Mohanty¹, and Matthias Katzfuss²**

4 ¹Biological and Agricultural Engineering, Texas A&M University, College Station,
5 Texas, USA

6 ²Department of Statistics, Texas A&M University, College Station, Texas, USA.

7

8 Corresponding author: Binayak P. Mohanty (bmohanty@tamu.edu)

9 Corresponding author address: 301A Scoates Hall, Texas A&M University, College
10 Station, Texas, 77840, USA.

11 **Keywords:** data fusion, remote sensing, big data, soil moisture, geostatistics, multi-
12 scale, spatio-temporal data

13 **Abstract**

14 The past six decades has seen an explosive growth in remote sensing data across air,
15 land, and water dramatically improving predictive capabilities of physical models and
16 machine-learning (ML) algorithms. Physical models, however, suffer from rigid
17 parameterization and can lead to incorrect inferences when little is known about the
18 underlying physical process. ML models, conversely, sacrifice interpretation for
19 enhanced predictions. Geostatistics are an attractive alternative since they do not have
20 strong assumptions like physical models yet enable physical interpretation and
21 uncertainty quantification. In this work, we propose a novel multiscale multi-platform
22 geostatistical algorithm which can combine big environmental datasets observed at
23 different spatio-temporal resolutions and over vast study domains. As a case study, we
24 apply the proposed algorithm to combine satellite soil moisture data from Soil Moisture
25 Active Passive (SMAP) and Soil Moisture and Ocean Salinity (SMOS) with point data
26 from U.S Climate Reference Network (USCRN) and Soil Climate Analysis Network
27 (SCAN) across Contiguous US for a fifteen-day period in July 2017. Using an
28 underlying covariate-driven spatio-temporal process, the effect of dynamic and static
29 physical controls—vegetation, rainfall, soil texture and topography—on soil moisture is
30 quantified. We successfully validate the fused soil moisture across multiple spatial
31 scales (point, 3 km, 25 km and 36 km) and compute five-day soil moisture forecasts
32 across Contiguous US. The proposed algorithm is general and can be applied to fuse
33 many other environmental variables.

34

35 **1 Introduction**

36 On April 1, 1960, (National Aeronautics and Space Administration) NASA launched the
37 Television and Infrared Observation Satellite (TIROS 1) demonstrating that satellites
38 could observe weather patterns, marking the advent of remote sensing (RS) to observe
39 global environmental phenomena. Sixty years and the launch of several satellites later,
40 rapid progress has been made in observing Earth-system processes (across air, land,
41 and water) accompanied by an explosion in the availability of data. This so called “big
42 data” are often spatio-temporal (indexed by a spatial coordinate and a time stamp)
43 resulting in an increased interest in space-time problems in the past two decades
44 (Gelfand et al., 2010; Wikle et al., 2019). Usually, environmental data are 1) spatio-
45 temporally dependent, 2) available at multiple resolutions from various instruments,
46 and 3) observed with gaps and noise. It is unreasonable to expect one source of data to
47 fill all the gaps across space and time. However, combining multi-sensor data, while
48 accounting for individual strengths and weaknesses, can lead to novel insights into
49 Earth-system Science. Paradigms facilitating the fusion of disparate data while handling
50 the sheer size of datasets are thus critical.

51

52 RS data have traditionally been used to update the states and improve parameterization
53 of physically based models. Indeed, the assimilation of satellite data into numerical
54 weather prediction models led to the “quiet revolution” (Bauer et al., 2015) in global
55 weather prediction. Data assimilation has also found success in oceanography
56 (Evensen, 1994; Ghil & Malanotte-Rizzoli, 1991) and land-surface hydrology (Reichle et
57 al., 2002). Physical models are vital for predicting variables poorly observed by RS
58 platforms such as ocean mixed layer (Wang et al., 2000) and root-zone soil moisture

59 (SM) (Lievens et al., 2017). However, the rigid parameterization of physical models can
60 be a hindrance when knowledge of the underlying spatio-temporal process is
61 incomplete (Giroto et al., 2017). The resulting predictions can suffer from signatures of
62 strong (and sometimes incorrect) assumptions (Akbar et al., 2019). Moreover, RS
63 observations usually need to be pre-processed for correcting bias and scale-mismatch
64 before assimilation in the numerical model (Koster et al., 2009).

65
66 The recent decade has seen an incredible rise of Machine Learning (ML) in Earth-
67 System Sciences, which has been instrumental in improving predictive accuracy of
68 disparate physical processes (Camps-valls et al., 2013; Hengl et al., 2017; Jung et al.,
69 2010; Mao et al., 2019; Shi et al., 2017). Though classical ML models are inept at
70 accounting for spatio-temporal dependence, recent research in Deep Learning seems
71 promising (Fang et al., 2017; Shen, 2018; Shi et al., 2017). Accuracy without
72 interpretability, however, is insufficient (Reichstein et al., 2019); the lack of transparency
73 and physical interpretability of many ML models is viewed as a major deficiency.
74 Moreover, current state-of-the-art ML models are ill-equipped to handle some of the
75 major challenges associated with fusing RS data such as accounting for multi-sensor
76 multiscale data, uncertainty in observations and predictions, and missing data
77 (Reichstein et al., 2019).

78
79 On an interpretation-prediction spectrum, physical models derived from the first laws
80 of physics lie on one end while ML algorithms using black-box models fall on the other.
81 Geostatistics lie somewhere in the middle and are an attractive alternative for spatio-
82 temporal inference in a data-driven setting. They do not have strong assumptions like
83 physical models yet enable physical interpretation and uncertainty quantification. From

84 its humble origins in South African mines (Cressie, 1990; Krige, 1952), geostatistics has
85 been widely used in modeling the spatio-temporal distribution of environmental
86 variables including precipitation (Cecinati et al., 2017), temperature (Lanfredi et al.,
87 2015), soil properties (Lark, 2012; Mohanty et al., 1991, 1994; Mohanty & Kanwar, 1994),
88 carbon dioxide (Zhong & Carr, 2019), ground-water quality (Goovaerts et al., 2005) and
89 SM (Joshi & Mohanty, 2010; Kathuria et al., 2019a; Mohanty et al., 2000). Recent work on
90 covariate-driven non-stationary models have also enabled the seamless integration of
91 covariates into geostatistical models (Reich et al., 2011; Risser & Calder, 2015) enabling
92 them to model complex spatio-temporal phenomena.

93
94 Geostatistical approaches typically assume an underlying Gaussian process (GP)
95 requiring quadratic memory and cubic time complexity in the number of observations,
96 which make them prohibitive as the data size increases. Various approximations have
97 therefore been proposed for applying geostatistics to massive datasets. Such approaches
98 generally aim at approximating the covariance (e.g., Kaufman et al., 2008) and inverse-
99 covariance matrices (e.g., Nychka et al., 2015). Among these, the *Vecchia* approximation
100 (Vecchia, 1988) is one of the oldest with several advantages such as it is 1) suitable for
101 high-performance parallel computing, 2) accounts for uncertainty in predictions, and 3)
102 outperforms several state-of-the-art approaches in accuracy (Guinness, 2018). Moreover,
103 recent work (Katzfuss et al., 2020; Katzfuss & Guinness, 2017) has shown that *Vecchia*
104 approximation can be generalized to include many existing GP approximation
105 approaches as special cases. However, the use of the *Vecchia* approximation, to the best
106 of the authors' knowledge, has been restricted to single-scale data only.

107

108 Thus, the objective of this paper is to investigate whether geostatistics, with its rich
109 parametric inference and uncertainty quantification, can potentially be used with
110 *Vecchia* approximation to fuse spatio-temporal multiscale big data.. We achieve this by
111 applying the *Vecchia* approximation to a geostatistical hierarchical model (Gelfand et al.,
112 2001; Kathuria et al., 2019b). In this paper, we define the term “multiscale big data” as
113 data which are observed from multiple platforms at varying footprints, are massive in
114 size, and are observed over vast extents rendering standard geostatistical (and many
115 other statistical) approaches infeasible.

116

117 We explore the utility of the approximation using simulations, and by fusing real SM
118 datasets as a case study. SM is a critical variable governing land-atmosphere
119 interactions and contains significant information about physical processes such as
120 rainfall (Koster et al., 2016), streamflow (Koster et al., 2018) and evapotranspiration (ET)
121 (Akbar et al., 2019). SM is highly correlated in space and time resulting from dynamic
122 interactions between surface and atmospheric controls making it a prime candidate for
123 geostatistics driven multiscale data fusion. Kathuria et al. (2019b) previously proposed
124 a geostatistical data fusion scheme for combining multiscale SM data but its application
125 was restricted to regions with small extent and small data size limiting its utility. We
126 also choose SM as a case study application for our proposed algorithm to provide a big
127 data closure for Kathuria et al. (2019b). The rest of the paper is organized as follows. We
128 describe the SM datasets used in the case study in Section 2. The data fusion algorithm
129 along with its big data extension is detailed in Section 3. This is followed by the
130 discussion of results in Section 4 before we conclude in Section 5. Note that in the
131 following sections, all vectors are assumed to be column vectors.

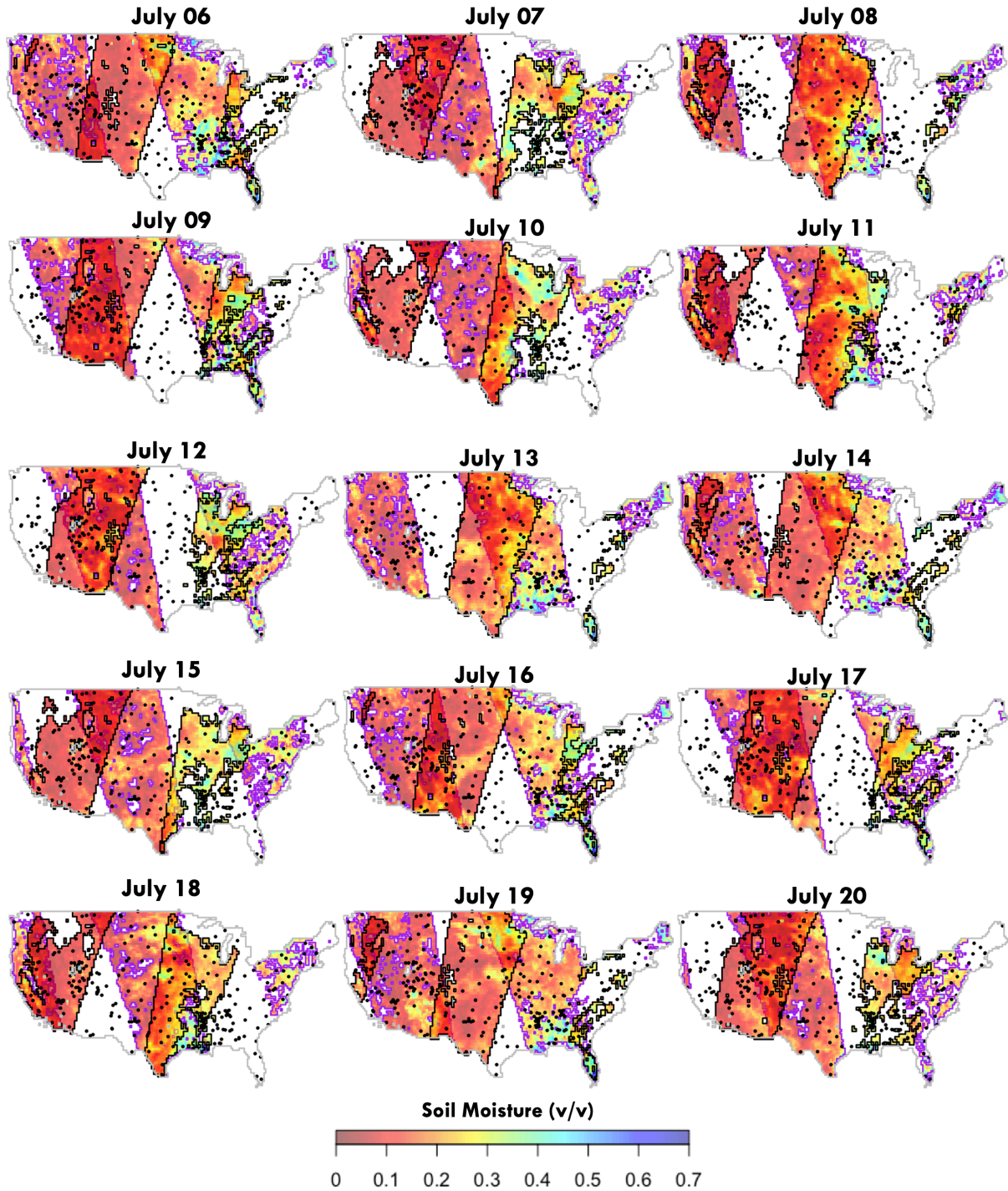
132

133 2 Study Area and Data

134 2.1 Case Study: Soil moisture

135 We apply the proposed algorithm to combine daily point surface (top 0-5 cm) SM data
136 from U.S. Climate Reference Network (USCRN) (Diamond et al., 2013) and Soil Climate
137 Analysis Network (SCAN) (Schaefer et al., 2007) with satellite data from Soil Moisture
138 Ocean Salinity (SMOS) (Barré et al., 2008) and Soil Moisture Active Passive (SMAP)
139 (Entekhabi et al., 2010) for Contiguous US (CONUS) for July 06-20, 2017. This fifteen-
140 day time interval was randomly chosen for the warm summer period so that the effect
141 of snow on SM estimation is minimal. For any given day, there are approximately 143
142 sites for USCRN and SCAN while individual satellites partially observe SM across
143 CONUS with some overlap between the two data sets (Figure 1).

144
145 Both SMOS and SMAP use L-band radiometers to measure surface brightness
146 temperature (T_b) at an average revisit time of three days (Colliander et al., 2017; Pablos
147 et al., 2019). Both the satellites apply (different) retrieval algorithms to T_b and generate
148 composite daily L3 SM products resampled, at 36 km for SMAP (L3) and 25 km for
149 SMOS (Barcelona Expert Center L3), to an Equal Area Scalable Earth (EASE)-2 grid. For
150 the SMAP data we remove the pixels where 1) the retrieval was unsuccessful (using flag
151 data), and 2) where the vegetation water content is greater than 5 kg/m^2 (O'Neill et al.,
152 2018). For consistency we use the morning overpass for both satellites— 6 AM local
153 time. For the covariate data, daily rainfall data were extracted from Parameter-elevation
154 Regressions on Independent Slopes Model (PRISM) at 4 km resolution. PRISM provides
155 gridded rainfall data across CONUS at a daily scale using a combination of
156 climatological and statistical methods (Daly et al., 1994). Soil and elevation data were



157
158

Figure 1. Fifteen day soil moisture data from USCRN and SCAN (black cross), SMOS (swath - black outline) and SMAP (swath - purple outline) for July 06-20, 2017. For individual days, both SMOS and SMAP observe different regions of Contiguous US (CONUS) and there is a significant overlap between the data. The size of the SM data and the extent of study domain (CONUS) are both massive making data fusion computationally demanding.

159 extracted from Soil Survey Geographic Database (1 km) (Soil Survey Staff, 2020) and
 160 Leaf Area Index (LAI) (as a proxy for vegetation) were extracted from Moderate
 161 Resolution Imaging Spectroradiometer (MCD15A3H, 500m) (Myneni et al., 2015).

162

163 **3 Methodology**

164 **3.1 Multiscale data fusion**

165 Let the environmental variable varying across space and time (such as SM, ET,
 166 temperature, etc.) be denoted by y . We assume that $y(\cdot)$ is a Gaussian Process (GP) (a
 167 standard geostatistical assumption) at the point scale in a domain or extent \mathfrak{D} in d
 168 dimensions ($d = 1, 2, 3 \dots$). For instance, if y represents daily land-surface temperature
 169 (LST) varying spatially (latitude and longitude) and temporally (days), then d equals 3.

170 The variable y is defined at the point scale using a mean function μ and a covariance
 171 function C :

172

$$173 \quad y(\cdot) \sim GP(\mu, C). \quad (1)$$

174

175 For any environmental variable y , in addition to point data, we might observe data at
 176 aggregate resolutions from RS platforms or large-scale numerical models. For instance,
 177 surface SM is observed at aggregate resolutions from SMAP ($\sim 36 \text{ km} \times 36 \text{ km}$, daily)
 178 and SMOS ($\sim 25 \text{ km} \times 25 \text{ km}$, daily) while ET is observed using ECOSTRESS (\sim
 179 $70 \text{ m} \times 70 \text{ m}$, daily) and MODIS ($\sim 500 \text{ m} \times 500 \text{ m}$, 8-day). Since y is defined at point
 180 scale, for any aggregate pixels A_i and A_j , $y(A_i) = \frac{1}{|A_i|} \int_{A_i} y(s) ds$, with the corresponding
 181 mean and covariance as:

182

183
$$\mu(A_i) = \frac{1}{|A_i|} \int_{A_i} \mu(s) ds \text{ and}$$

184
$$C(A_i, A_j) = \frac{1}{|A_i|} \frac{1}{|A_j|} \int_{A_i} \int_{A_j} C(s_1, s_2) ds_1 ds_2, \quad (2)$$

185

186 where $|A_i|$ is the d -dimensional resolution of pixel A_i and s represents a point in d
 187 dimensions. If A_i and A_j represent coordinates of point data, the mean of data at A_i is
 188 simply $\mu(A_i)$ and the covariance between A_i and A_j is given as $C(A_i, A_j)$. If A_i is an areal
 189 pixel and A_j represents a point, then the covariance $C(A_i, A_j)$ is given as $\frac{1}{|A_i|} \int_{A_i} C(s, A_j) ds$.

190

191 Let the total number of observed pixels be n and be denoted by $\mathcal{A} = \{A_1, \dots, A_n\}$ with
 192 $A_i \subset \mathfrak{D}$. The joint distribution of $y(\mathcal{A}) = (y(A_1), \dots, y(A_n))$ can be shown to be
 193 multivariate normal (Gelfand et al., 2001):

194

195
$$y(\mathcal{A}) = \mathcal{N}_n(\mu(\mathcal{A}), C(\mathcal{A}, \mathcal{A})), \quad (3)$$

196

197 where $\mu(\mathcal{A})$ is a vector of length n and $C(\mathcal{A}, \mathcal{A})$ is a matrix of size $n \times n$. The
 198 individual elements of $(\mu(\mathcal{A}))_i$ and $(C(\mathcal{A}, \mathcal{A}))_{ij}$ are given by equation 2. Since we
 199 cannot always analytically solve the above integrals, we use a numerical approximation
 200 (Gelfand et al., 2001) by assuming an equidistant numerical grid \mathcal{G} over the extent \mathfrak{D}
 201 with $n_{\mathcal{G}}$ number of grid points such that $\mathcal{G} = \{g_1, \dots, g_{n_{\mathcal{G}}}\}$ or equivalently $\mathcal{G} = \{g_k : k =$
 202 $1, \dots, n_{\mathcal{G}}\}$. Here g_k denotes the location of the k^{th} grid point in \mathcal{G} . We can then
 203 approximate $y(A_i)$ as:

204

$$y(A_i) \approx \frac{1}{n_{A_i}} \sum_{g_k \in \mathcal{G}_{A_i}} y(g_k), \quad (4)$$

206

207 where \mathcal{G}_{A_i} denotes the subset of the total grid points \mathcal{G} lying inside the pixel A_i , and
 208 n_{A_i} denotes the number of grid points in \mathcal{G}_{A_i} . The corresponding approximations for the
 209 mean and covariance can be written as:

210

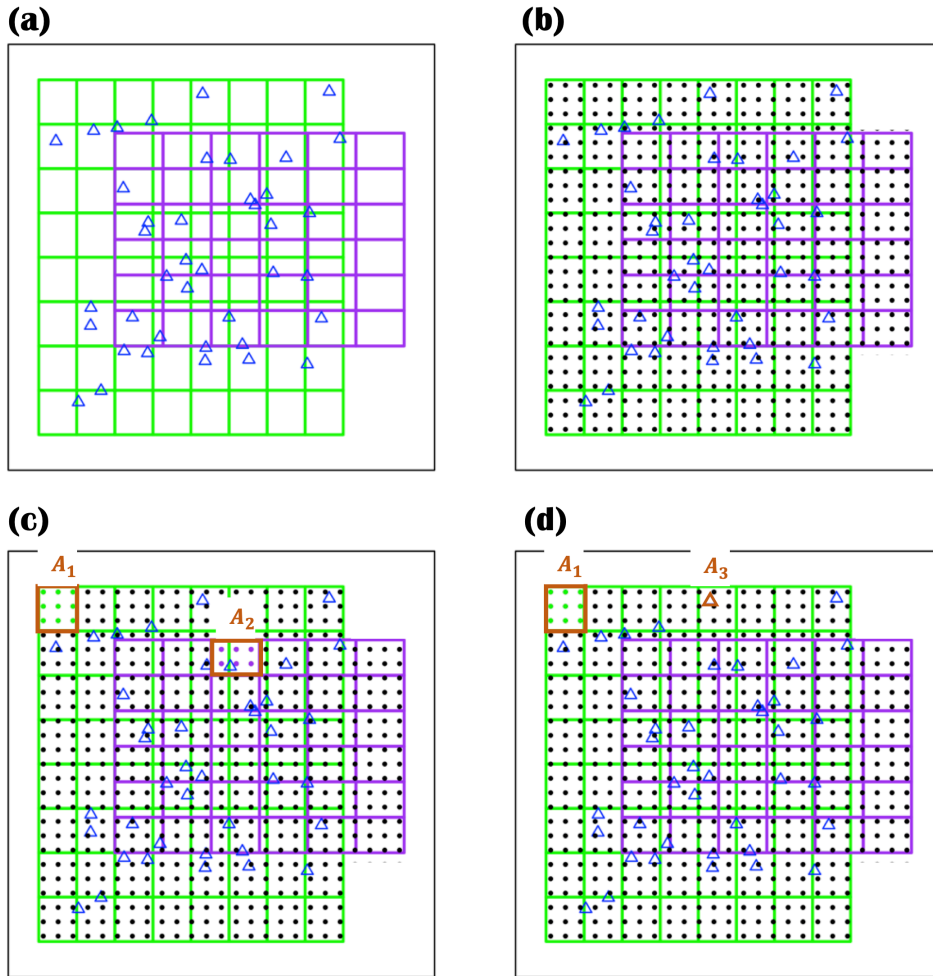
$$\begin{aligned} 211 \quad \mu(A_i) &\approx \frac{1}{n_{A_i}} \sum_{g_k \in \mathcal{G}_{A_i}} \mu(g_k), \\ 212 \quad C(A_i, A_j) &\approx \frac{1}{n_{A_i}} \frac{1}{n_{A_j}} \sum_{g_k \in \mathcal{G}_{A_i}} \sum_{g_l \in \mathcal{G}_{A_j}} C(g_k, g_l). \end{aligned} \quad (5)$$

213

214 We illustrate the numerical approximation using a hypothetical example in Figure 2.
 215 Figure 2 (a) represents three partially overlapping datasets which cover different
 216 extents and have different resolutions: two areal datasets R_1 (64 green pixels) and R_2 (36
 217 purple pixels), and point dataset P_1 (40 blue triangles). Figure 2 (b) represents the
 218 equidistant grid \mathcal{G} (black dots) over the study domain. Assuming the mean and
 219 covariance functions are known at the point scale, the mean of pixel A_1 (A_2) and the
 220 covariance between pixels A_1 and A_2 in Figure 2 (c) are given by equation 5. Here
 221 \mathcal{G}_{A_1} (\mathcal{G}_{A_2}) are subset of the total grid points \mathcal{G} , color-coded as green (purple), lying inside
 222 A_1 (A_2) with $n_{A_1} = 9$ ($n_{A_2} = 6$). Similarly, the mean function at point A_3 in Figure 2 (d) is
 223 simply given as $\mu(A_3)$ while $C(A_1, A_3)$ is given by $\frac{1}{n_{A_1}} \sum_{g_k \in \mathcal{G}_{A_1}} C(g_k, A_3)$.

224

225



226
227

Figure 2. (a) Example depicting two areal (green and purple) and one point (blue triangles) data platforms (b) Equidistant point grid assumed throughout the study domain (c) The mean and covariance of pixels A_1 and A_2 approximated using the numerical grid (d) The mean and covariance between a pixel A_1 and point observation A_3 .

228 We can write $\frac{1}{n_{A_i}} \sum_{g_k \in \mathcal{G}_{A_i}} y(g_k)$ (equation 4) in matrix form as $h_{A_i}^T y_{A_i}$, where h_{A_i} is a vector of
 229 length n_{A_i} with each element equal to $1/n_{A_i}$ or $h_{A_i} = (1/n_{A_i}, \dots, 1/n_{A_i})$, and y_{A_i} is a
 230 vector of length n_{A_i} with elements $\{y(g_k): g_k \in \mathcal{G}_{A_i}\}$. Similarly in equation 5, $\mu(A_i)$ can be
 231 written as $h_{A_i}^T \mu_{A_i}$ (with μ_{A_i} having elements $\{\mu(g_k): g_k \in \mathcal{G}_{A_i}\}$). We also write $C(A_i, A_j)$ in
 232 equation 5 in matrix form as $h_{A_i}^T (C(\mathcal{G}_{A_i}, \mathcal{G}_{A_j})) h_{A_j}$, where (as mentioned before) \mathcal{G}_{A_i}
 233 denotes the subset of the total grid points \mathcal{G} lying inside the pixel A_i .

234

235 Retrievals of an environmental variable from different platforms are typically subject to
 236 systematic (bias) and stochastic (random) errors (e.g. refer Fan et al. (2020) and Reichle
 237 & Koster (2004) for SM, Li et al. (2014) and Westermann et al. (2012) for LST, Klees et al.
 238 (2007) for water storage, Hu et al. (2015) and Velpuri et al. (2013) for ET). Thus, for any
 239 observed pixel A_i , it is important to differentiate between the noisy observation from a
 240 platform (denoted as $z(A_i)$) and the latent environmental variable $y(A_i)$ that is
 241 uncorrupted by the parameterized errors. For a given observation $z(A_i)$ (from a data
 242 platform) for pixel A_i , we thus write:

243

$$244 \quad z(A_i) = y(A_i) + \delta(A_i) + \kappa(A_i)y(A_i) + \epsilon(A_i), \quad (6)$$

245

246 where $\delta(A_i)$, $\kappa(A_i)$ and $\epsilon(A_i)$ are respectively the additive bias, multiplicative bias, and
 247 random measurement error associated with $z(A_i)$. We parameterize the random error as
 248 $\epsilon(A_i) \sim \mathcal{N}(0, \tau_{A_i}^2)$ with variance $\tau_{A_i}^2$. We then write:

249

$$\begin{aligned}
 250 \quad z(A_i) &\approx h_{A_i}^T y_{A_i} + \delta(A_i) + \kappa(A_i) h_{A_i}^T y_{A_i} + \epsilon(A_i) \\
 251 \quad &= (1 + \kappa(A_i)) h_{A_i}^T y_{A_i} + \delta(A_i) + \epsilon(A_i) \\
 252 \quad &= (h_{A_i}^\kappa)^T y_{A_i} + \delta(A_i) + \epsilon(A_i), \tag{7}
 \end{aligned}$$

253 where $h_{A_i}^\kappa = (1 + \kappa(A_i)) h_{A_i}^T$. The mean (μ) and covariance function (C) in equation 1 are
 254 thus given parametric forms based on the environmental variable y while the additive
 255 bias ($\delta(A_i)$), multiplicative bias ($\kappa(A_i)$) and error-variance ($\tau_{A_i}^2$) for a pixel A_i in
 256 equation 7 are parameterized depending on the data platforms. Let all the parameters
 257 used to parameterize the mean, covariance, bias and random error be denoted by the
 258 vector θ . Elements of θ can either assumed to be known or be estimated from the
 259 observations. If the total number of observations from all platforms is equal to n , we
 260 denote $z(\mathcal{A}) = \{z(A_1), z(A_2), \dots, z(A_n)\}$. The parameter vector θ is estimated by
 261 maximizing the likelihood $f(z(\mathcal{A})|\theta)$ where $f(A|B)$ denotes the probability density of A
 262 given B . For our model, it can be easily derived that the (log-) likelihood is:

$$263 \quad -2\log(f(z(\mathcal{A})|\theta)) = \log(\det(\Sigma_z)) + (z(\mathcal{A}) - \mu_z)^T \Sigma_z^{-1} (z(\mathcal{A}) - \mu_z) + n\log(2\pi), \tag{8}$$

264
 265 where the i^{th} element of the vector μ_z (size n) and the $(i, j)^{th}$ element of the matrix Σ_z
 266 (size $n \times n$) in equation 8 are given as:

$$\begin{aligned}
 268 \quad \mu_{z,i} &\approx (h_{A_i}^\kappa)^T \mu_{A_i} + \delta(A_i), \\
 269 \quad \Sigma_{z,ij} &\approx (h_{A_i}^\kappa)^T (C(\mathcal{G}_{A_i}, \mathcal{G}_{A_j})) h_{A_j}^\kappa + \tau_{A_i,j}^2, \tag{9}
 \end{aligned}$$

270

271 where $\tau_{A_{i,j}}^2 = \begin{cases} \tau_{A_i}^2, & i = j \\ 0, & i \neq j \end{cases}$. However this data fusion algorithm becomes computationally
 272 infeasible when the size of the datasets and/or the extent of study domain becomes
 273 large. We therefore propose an approximation to the fusion algorithm for such cases in
 274 the next Section.

275

276 **3.2 Vecchia-multiscale: An Approximation for Multiscale Big Data**

277 If the total number of observations (governed by the number of data platforms and
 278 resolution of pixels for a given study domain) be n , and the number of assumed grid
 279 points (governed by the extent of the study domain and distance between individual
 280 grid points) be n_G , then computing Σ_z and finding its inverse Σ_z^{-1} in equation 8 requires
 281 $\mathcal{O}(n_G^2) + \mathcal{O}(n^3)$ floating point operations. This evaluation becomes computationally
 282 prohibitive as the number of data and the size of study domain increase (e.g., when
 283 combining multiple data platforms for continental scale fusion of an environmental
 284 variable), and thus requires an approximation. To approximate the likelihood, we first
 285 write the joint distribution in $f(z(\mathcal{A})|\theta)$ as a product of univariate conditional
 286 distributions as

$$287 \quad f(z(\mathcal{A})|\theta) = f(z(A_1)|\theta) \times \prod_{i=2}^n f(z(A_i)|\mathbf{z}(\mathbf{A}_{1:i-1}), \theta), \quad (10)$$

288 where $\mathbf{A}_{1:i-1}$ denotes $\{A_1, \dots, A_{i-1}\}$ and thus $\mathbf{z}(\mathbf{A}_{1:i-1})$ denotes $\{z(A_1), \dots, z(A_{i-1})\}$.

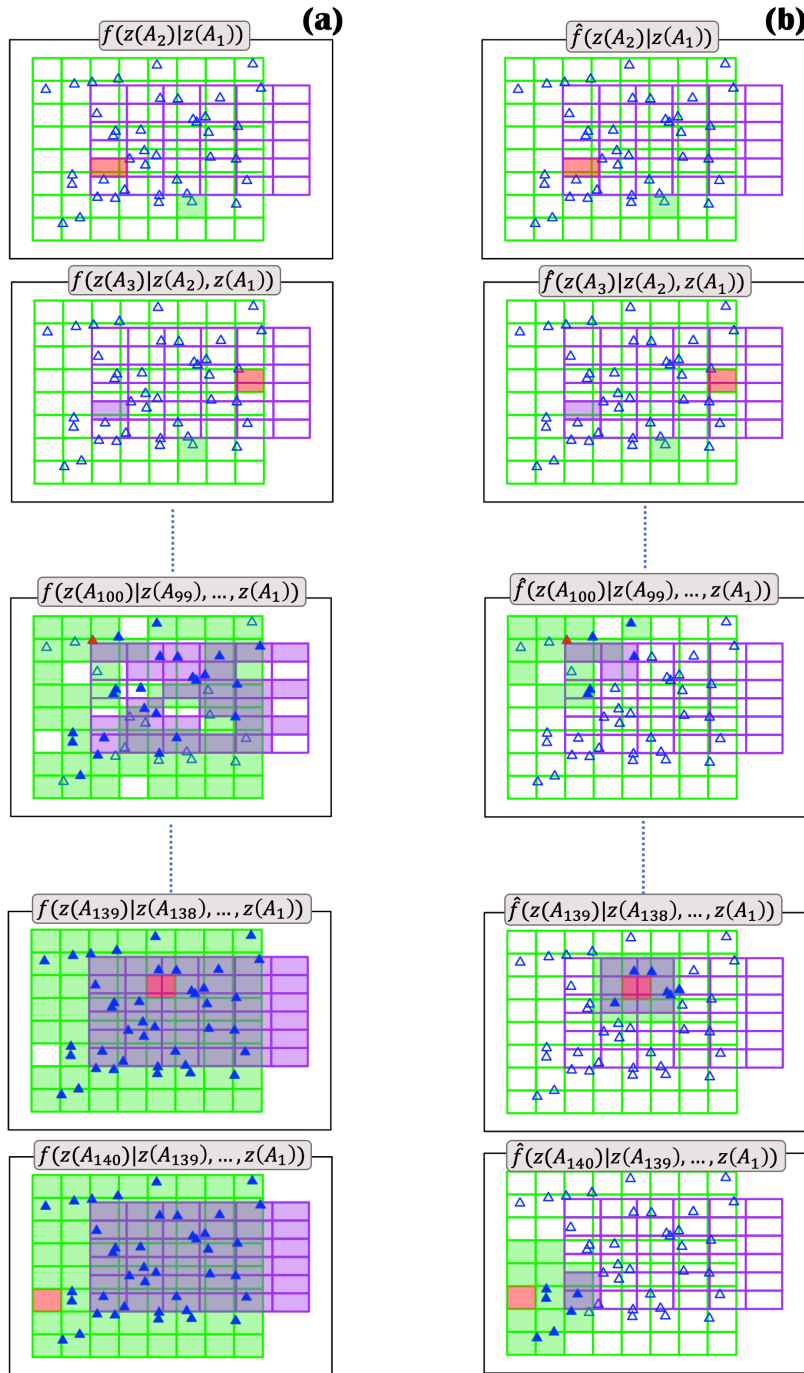
289 Following Vecchia (1988) we approximate the likelihood $f(z(\mathcal{A})|\theta)$ as:

290

$$291 \quad \hat{f}(z(\mathcal{A})|\theta) = f(z(A_1)|\theta) \times \prod_{i=2}^n f(z(A_i)|\mathbf{z}(\mathbf{A}_{m_i}), \theta), \quad (11)$$

292

293 where \mathbf{A}_{m_i} is a subvector of $\mathbf{A}_{1:i-1}$ of length m_i such that $m_i = \begin{cases} i - 1, & i \leq m \\ m, & i > m \end{cases}$. Here m is
294 an integer lying between 1 and $n - 1$ with $m = n - 1$ representing the exact likelihood
295 in equation 10. The elements of subvector \mathbf{A}_{m_i} consist of m_i elements from $\mathbf{A}_{1:i-1}$ which
296 are closest to A_i in space. The subvector $\mathbf{z}(\mathbf{A}_{m_i})$ is the observed data vector
297 corresponding to \mathbf{A}_{m_i} . To illustrate the approximation, we again use the hypothetical
298 example in Figure 2 (a) comprising three datasets: areal data R_1 (64 green pixels) and R_2
299 (36 purple pixels), and point data P_1 (40 blue triangles), making the total number of
300 observations $n = 140$. For this data, the univariate conditional distributions are
301 illustrated in Figure 3 using a random permutation of the pixels \mathcal{A} and choosing $m =$
302 20. Column (a) presents the conditional distributions in equation 10 corresponding to
303 the exact likelihood while column (b) consist of the corresponding conditional
304 distributions resulting from the *Vecchia* approximation. The i^{th} pixel A_i in equations 10
305 and 11 (where $i = 2, \dots, 140$ increases from top to bottom in the columns) is color-filled
306 in red while the pixels (or points) of the conditioning vector $\mathbf{z}(\mathbf{A}_{1:i-1})$ (equation 10) or
307 $\mathbf{z}(\mathbf{A}_{m_i})$ (equation 11) are color-filled in green (R_1), purple (R_2) and blue (P_1). It can be
308 seen in Figure 3 that for $i > m$, the *Vecchia* approximation selects a subset of m pixels
309 (or points) for each A_i . It can be shown that this approximation is equivalent to inducing
310 sparsity (large percentage of zeros) in the inverse Cholesky factor matrix Λ ($\Lambda^T \Lambda = \Sigma_z^{-1}$).
311 This leads to fast evaluation of Σ_z^{-1} (and consequently the likelihood) in equation 8 used
312 for estimating the parameter vector θ as well as doing subsequent predictions. The
313 detailed algorithm for parameter estimation and subsequent predictions is given in
314 Appendix A1. We call this approximation *Vecchia-multiscale*.



315

Figure 3. Illustration of the Vecchia-multiscale to the hypothetical data in Figure 2(a) consisting of 64 green pixels (R_1), 36 purple pixels (R_2) and 40 point data P_1 (blue triangles). Column (a) denotes the conditional distributions as implied by the the exact likelihood while column (b) gives the conditional distributions using Vecchia-multiscale approximation with maximum size of the conditioning vector m equal to 20. The i^{th} pixel A_i (where $i = 2, \dots, 140$ increases from top to bottom in the columns) is color-filled in red while the pixels (or points) of the conditioning vector are color-filled in green (R_1), purple (R_2) and blue (P_1).

316 **3.2.1 Permutation in Vecchia-multiscale**

317 There are two criteria we seek in the approximation: speed and accuracy. For the
 318 *Vecchia-multiscale*, significant computational and memory benefits can be achieved by
 319 selecting $m \ll n$. Further, equation 11 results in a product of independent univariate
 320 distributions which is readily parallelized for faster computations.

321
 322 Regarding accuracy for a fixed value of m , as the right side of equation 11 consists of an
 323 “ordered” sequence of conditional probability distributions, the approximation
 324 depends on the order in which the pixels appear in \mathcal{A} . This is because in equation 11,
 325 for a pixel A_i ($i \geq 2$), we select the subset \mathbf{A}_{m_i} (of length m_i) from elements of
 326 $\mathbf{A}_{1:i-1}$ which are closest in space to A_i . This leads to different values for $\mathbf{z}(\mathbf{A}_{m_i})$ in
 327 equation 11 based on how we permute $\{A_1, \dots, A_n\}$. Thus, the approximation accuracy
 328 will depend upon what permutation of $\{A_1, \dots, A_n\}$ we choose for the pixels (and points)
 329 for computing $\hat{f}(z(\mathcal{A})|\theta)$ in equation 11. When the size of the multiscale data is
 330 massive, it is infeasible to explore all such permutations. For point data, Guinness (2018)
 331 found that certain permutations of \mathcal{A} give more accurate approximations when
 332 compared with the exact likelihood $f(z(\mathcal{A})|\theta)$. In this paper we explore the same for
 333 multiscale data. We use four popular permutations (Guinness, 2018): 1) *Joint-Coordinate*
 334 (ordering the locations based on increasing coordinate values), 2) *Joint-Middleout*
 335 (ordering locations based on increasing distance to the mean location of the extent), 3)
 336 *Joint-Maxmin* (ordering in which each successive point is chosen to “maximize the
 337 minimum distance” to previously selected points), and 4) *Joint-Random* (randomly

338 ordering locations). Interested readers are encouraged to refer to Section S1, Supporting
339 Information (SI) and Guinness (2018) for details on these permutations.

340

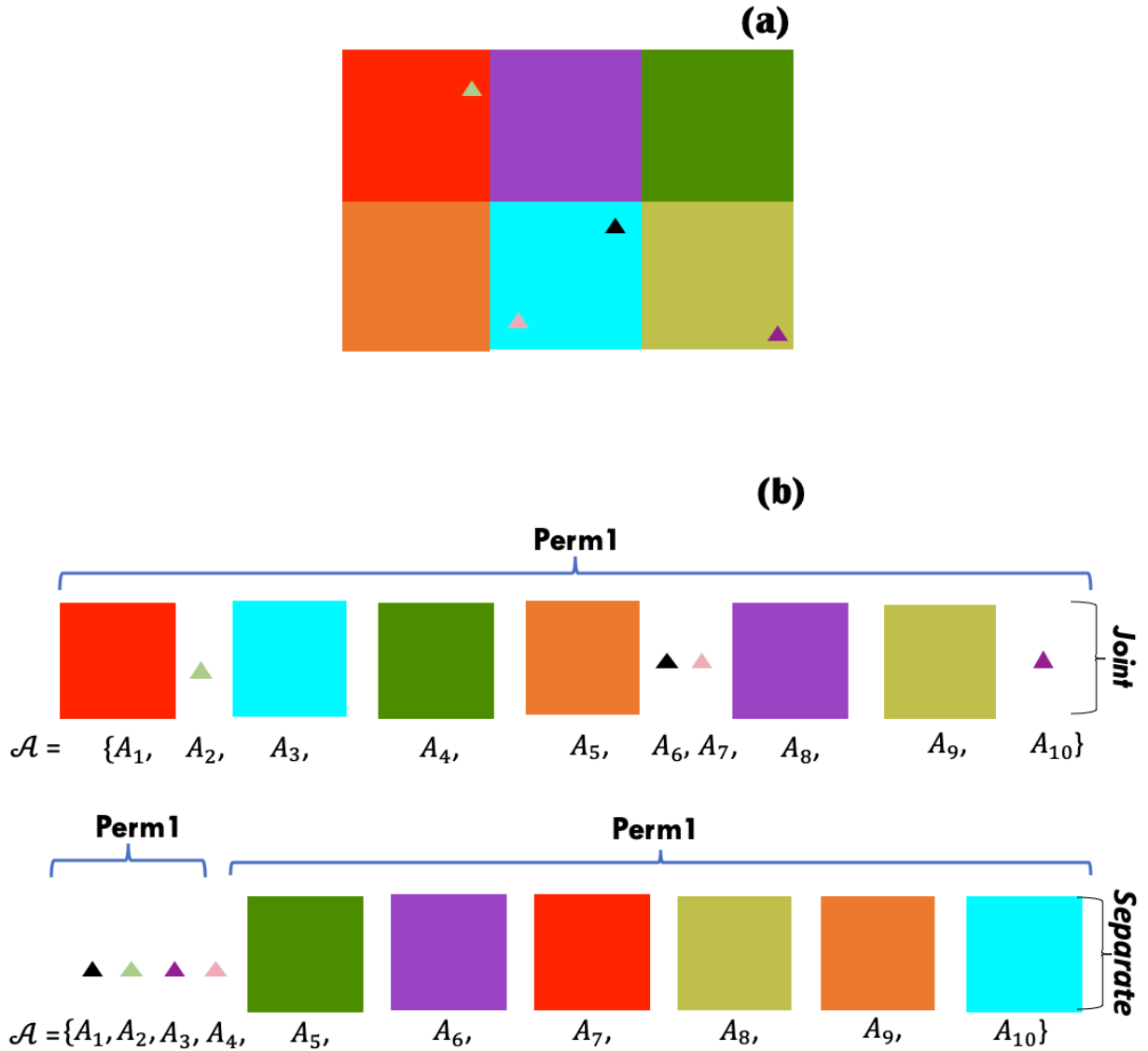
341 In addition to the above “Joint-” permutations, we introduce “Separate-” permutations
342 where we first separate out the point and areal data and apply the above-mentioned
343 four permutations separately to each. We then form the final permutation by sorting the
344 “ordered” point data followed by the “ordered” areal data. This leads to four additional
345 corresponding permutations: 5) *Separate-Coordinate*, 6) *Separate-Middleout*, 7) *Separate-*
346 *Maxmin*, and 8) *Separate-Random*. The difference between “Joint-” and “Separate-”
347 permutations is illustrated in Figure 4. We assume the centroid of an areal pixel as its
348 location for applying the permutations.

349

350 Using the hypothetical example in Figure 2 (a), we illustrate the effect of these eight
351 chosen permutations (Section S1, SI) on how the pixels and points are ordered in \mathcal{A} and
352 how it affects the evaluation of $\hat{f}(z(\mathcal{A})|\theta)$. To see which permutation performs better
353 for the *Vecchia-multiscale* in general, we use simulated data in two (e.g., a variable
354 varying across latitude and longitude) and three (e.g., a variable varying across latitude,
355 longitude and time) dimensions. The details of the simulations and the corresponding
356 results are given in Section S2, SI.

357

358 For both two and three dimensions, in general, the *Separate-Maxmin* and *Separate-*
359 *Random* perform the best while the *Coordinate-based* orderings perform the worst. This is
360 important because many approximation schemes use *Coordinate-based ordering* as their
361 default (e.g. Datta et al., 2016; Sun & Stein, 2016) and it should be used with caution



362

Figure 4. Illustration of “Joint-” and “Separate-” permutations for Vecchia-multiscale. (a) Hypothetical example comprising six aggregate pixels and four point data. Different colors are used to distinguish between different pixels and points. (b) The “Joint-” permutation results in both the pixels and points getting permuted together following a given permutation “Perm1”. For “Separate-” ordering, we first separate the point and aggregate data, apply the permutation “Perm1” separately to each, and then form the final permutation by sorting the permuted point data followed by the permuted aggregate data. In this figure we choose a random permutation as “Perm1” and the resulting permutations of the pixels/points are shown. The “Joint-” and “Separate-” permutations can lead to different ordering of the pixels/points in $\mathcal{A} = \{A_1, \dots, A_{10}\}$ resulting in different values of the approximate likelihood computed using Vecchia-multiscale. In this paper, we explore “Coordinate”, “Middleout”, “Maxmin” and “Random” as possible permutations for “Perm1”. The centroid of an aggregate pixel is chosen as its location for permutations.

363 when using *Vecchia-multiscale*. The subvector \mathbf{A}_{m_i} (equation 11) consists of a good mix of
364 both far and near pixels as well as nearby point data for *Separate-Maxmin* (Figure S2 (i)-
365 (l), SI) and *Separate-Random* (Figure S2 (m)-(p), SI). We hypothesize that conditioning a
366 pixel/point on both near and far pixels help in better approximation of the exact
367 likelihood. Additionally, the “Separate-” permutations lead to the subvector \mathbf{A}_{m_i} consist
368 of nearby point data which is potentially helpful because 1) for a given study domain,
369 point data are generally sparse for any environmental variable and are generally (but
370 not always) considered more accurate than remote sensing data, and 2) we define our
371 model at the point scale (equation 1), and it is thus potentially helpful to condition
372 pixels/points on nearby point data.

373

374 We therefore suggest adopting *Separate-Maxmin* or *Separate-Random* when using *Vecchia-*
375 *multiscale*. Since, our aim is to propose a general algorithm, we only use location
376 information for permuting $\{A_1, \dots, A_n\}$. A promising area of future research is exploring
377 physically-based permutation of pixels based on the environmental variable to be fused.
378 In the next Section, we apply the *Vecchia-multiscale* to fuse multiscale SM data for
379 CONUS.

380 **4 Results and Discussion**

381 **4.1. Case Study : Soil moisture**

382 We fuse fifteen days of SMOS, SMAP, and point (USCRN and SCAN) SM data across
383 CONUS from July 06-20, 2017. We randomly hold-out 27 point stations ($\approx 20\%$) for
384 validation leaving 116 station data for training. Since SM observations are theoretically
385 bounded between 0 and 1 and exhibit considerable skewness, the Gaussian assumption

386 becomes untenable. We thus use a logit transform $SM' = \log\left(\frac{SM}{1-SM}\right)$ which transforms
387 the SM values to lie between $-\infty$ to ∞ and also make the distribution less skewed
388 (Figure S4, SI). Overlapping data from SMOS and SMAP during the analyzed period
389 also exhibit slightly better correlation on the transformed scale (Figure S5, SI).

390

391 **4.2.1 Mean, covariance and bias**

392 Numerous studies (Cosh & Brutsaert, 1999; Crow et al., 2012; Entin et al., 2000; Gaur &
393 Mohanty, 2013, 2016; Joshi et al., 2011; Joshi & Mohanty, 2010; Kathuria et al., 2019a;
394 Ryu & Famiglietti, 2006; Teuling & Troch, 2005; Vereecken et al., 2014) have found that
395 SM distribution across space and time is affected primarily by precipitation, soil texture,
396 topography and vegetation. Therefore, we model the spatio-temporal SM distribution
397 as a function of these physical covariates. For SMAP, since we only consider pixels
398 where SM retrieval was successful (from flag data) and have a vegetation water content
399 $\leq 5 \text{ kg/m}^2$, we assume that the SMAP data are of good quality and do not have any
400 bias. As we did not pre-filter SMOS data, we assume a constant additive and
401 multiplicative bias for SMOS. Exploratory analysis between overlapping SMOS-SMAP
402 pixels at the logit scale (Figure S5, SI) also suggest a (additive and multiplicative) bias
403 between the two platforms. We assume normally distributed measurement error (at the
404 transformed scale) with mean zero and variance τ_{SMAP}^2 and τ_{SMOS}^2 for the two platforms
405 respectively. Since the USCRN/SCAN data undergo rigorous quality control, we
406 assume point data to be the ground truth with no bias/error.

407

408 We use exploratory analysis for determining the parametric forms for the mean
409 function. Since we assume bias in SMOS data, we use only SMAP and point data for the

410 exploratory analysis. For the exploratory analysis, the covariates are linearly averaged
 411 to the SMAP resolution. For rainfall, we assume 3-day antecedent mean rainfall as a
 412 covariate. On the original scale (Figure 5 (a)), the relationship between SM and the
 413 physical controls is non-linear. But after some non-linear transformations of the
 414 covariates (and logit transform of SM), an approximate linear relationship between SM
 415 and the covariates can be assumed (Figure 5 (b)). The mean trend of SM can be therefore
 416 written as:

417

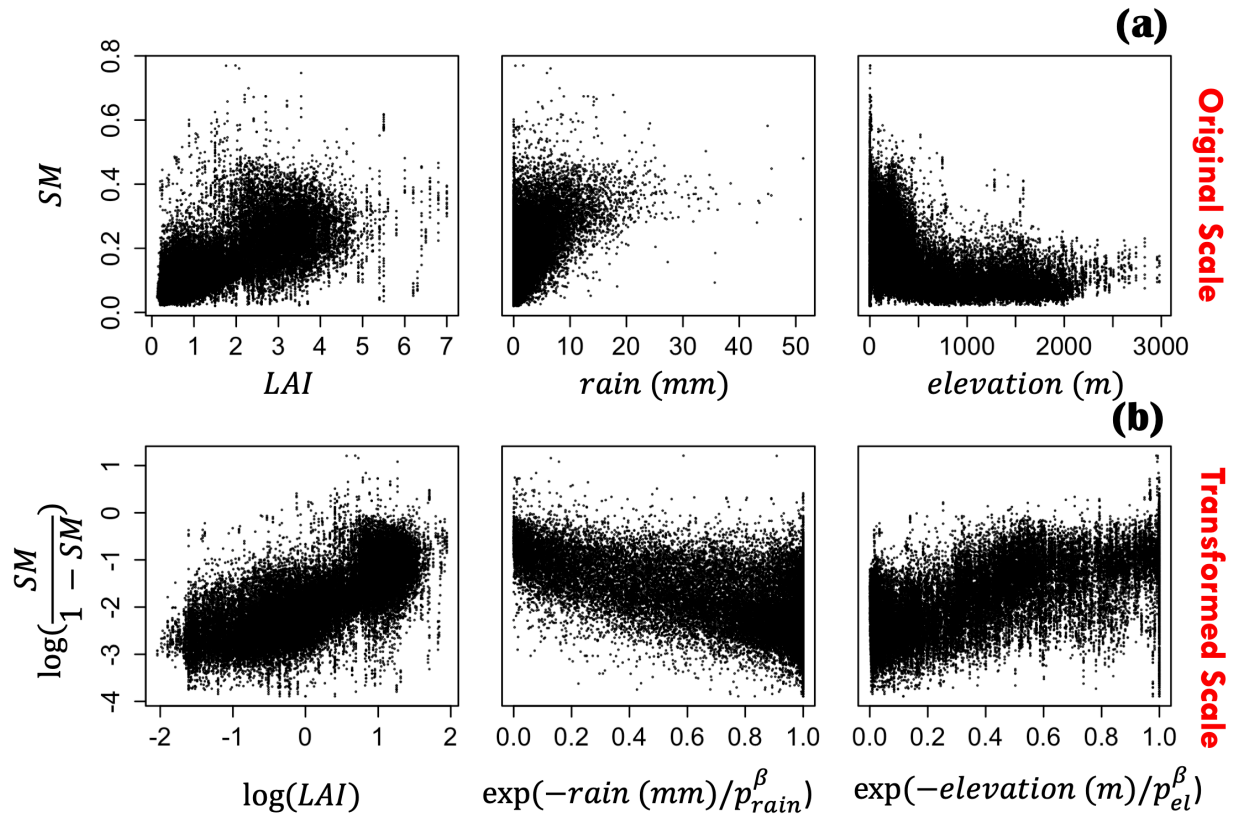
$$418 \quad \mu \left(\log \left(\frac{SM}{1-SM} \right) \right) = \mu(SM') = \beta_0 + \beta_1 \log(LAI) + \beta_2 \exp\left(-\frac{rain}{p_{rain}^\beta}\right) + \beta_3 \exp\left(-\frac{elevation}{p_{elevation}^\beta}\right). \quad (12)$$

419

420 We fix p_{rain}^β and $p_{elevation}^\beta$ as 3.3 mm and 342.6 m based on exploratory analysis. These
 421 two parameters represent the range of the exponential functions in equation 12 for
 422 which an approximate linear relationship holds between SM' and the transformed
 423 covariates in Figure 5 (b). Note that the covariates are resampled only for exploratory
 424 analysis and no resampling of (SM and covariate) data is required for implementing the
 425 actual algorithm in Section 3. Since we use an equidistant grid to approximate
 426 multiscale SM data, the grid points are assigned values according to the covariate pixels
 427 in which they lie. Though this results in grid points lying in a covariate pixel getting the
 428 same values, this allows us to work with covariate data at different resolutions and
 429 avoid errors introduced due to resampling of covariate data.

430

431 The covariance between any two points (x_1, y_1, t_1) and (x_2, y_2, t_2) , where x, y, t
 432 represent the latitude, longitude and time respectively, will also vary based on the
 433 underlying covariate heterogeneity and therefore the assumption of a stationary



434
435

Figure 5 Exploratory analysis of soil moisture with physical covariates. (a) The relationship of soil moisture with the physical covariates is non-linear on the original scale. (b) Appropriate covariate transformation results in an approximate linear relationship of SM (on the logit scale) with the physical covariates. The values of p_{rain}^β and $p_{elevation}^\beta$ are fixed as 3.3 mm and 342.6 m in the plots.

436 covariance function is too simplistic. Thus, for the covariance function C (equation 1),
 437 we use a non-stationary covariance function (Kathuria et al., 2019a; Reich et al., 2011)
 438 such that:

$$439 \quad C(SM'(x_1, y_1, t_1), SM'(x_2, y_2, t_2)) = C(s_1, s_2)$$

$$440 \quad = \sum_{j=1}^M w_j(X_{cov}(s_1))w_j(X_{cov}(s_2))C_j(|s_1 - s_2|). \quad (13)$$

441 The covariance function in equation 13 is a weighted sum of M isotropic covariance
 442 functions $\{C_j; j = 1, 2, \dots, M\}$ where the weights $\{w_j; j = 1, 2, \dots, M\}$ are a function of the
 443 underlying physical covariates $X_{cov}(s)$ affecting the covariance. The weighting
 444 functions w_j s are modeled using a multinomial logistic function of the underlying
 445 covariates: $w_j(s) = \frac{\exp(X_{cov}(s)^T \alpha_j)}{\sum_{l=1}^M \exp(X_{cov}(s)^T \alpha_l)}$. The details of the covariance function can be found
 446 in Reich et al. (2011) and Kathuria et al. (2019a). For our analysis, we choose exponential
 447 covariance functions (Matern with smoothness = 0.5) for individual C_j s (equation 13)
 448 with different range parameters for space (r_{xy}^j) and time (r_t^j) (e.g., Guinness, 2018):

$$450 \quad C_j(s_1, s_2) = \sigma_j^2 \exp\left(-\sqrt{\frac{\|(x_1, y_1) - (x_2, y_2)\|^2}{(r_{xy}^j)^2} + \frac{|t_1 - t_2|^2}{(r_t^j)^2}}\right). \quad (14)$$

451 We chose the exponential covariance functions for individual C_j s as changing the
 452 smoothness parameter for Matern resulted in insignificant change in the estimated
 453 maximum likelihood, and exponential functions are computationally faster to
 454 evaluate than Matern due to the added cost of evaluating the Bessel functions for the
 455 Matern function. We fix $M = 3$ to keep the number of parameters to be estimated
 456 relatively low. We include LAI, three-day mean antecedent rain, clay and elevation in

457 X_{cov} . As mentioned in Section 3, both the mean and covariance functions are defined at
458 point scale with computations at areal supports done as outlined in Section 3.1. In this
459 work, since point data are sparse, the parameter estimates of the mean and covariance
460 functions are expected to be mainly driven by SMAP and SMOS data. Note that we do
461 not include latitude, longitude or time as covariates in either the mean or covariance
462 function to make the fusion scheme more general and transferable.

463

464 **4.2.2 Parameter estimation and inference**

465 We assume a numerical grid \mathcal{G} (Section 3.1) spaced approximately 0.09 degrees apart
466 across the CONUS for each of the fifteen days resulting in close to 100,000 grid points
467 per day ($n_{\mathcal{G}} \approx 15 \times 100,000 = 1,500,000$). The total number of observations n from all
468 platforms (SMAP, SMOS, and USCRN/SCAN) for fifteen days equal 100,386. Parameter
469 estimation and subsequent predictions by computing exact likelihood is
470 computationally intractable for such a big dataset and thus requires an approximation.
471 We use the approximation detailed in Section 3 using the *Separate-Maxmin* orderings.
472 Since SMAP and SMOS observe SM at an interval of 3-7 days, we compute the *Separate-*
473 *Maxmin* ordering only considering the spatial coordinates (latitude and longitude) of
474 the data so that the temporal information of SM is also adequately represented in the
475 conditioning vector \mathbf{z}_{m_i} in equation 11. We fix the number of neighbors as $m = 60$; the
476 choice of m was taken to balance the predictive accuracy and computational speed. We
477 carry out parameter estimation using a global optimization algorithm called
478 Generalized Simulated Annealing (Xiang et al., 2013), a generalized and improved form
479 of simulated annealing, to find the parameter estimates that maximize the likelihood.

480

481 On the logit scale, the estimated mean parameters (equation 12) are $\beta = \{\beta_0, \beta_1, \beta_2, \beta_3\} =$
482 $\{-1.71, 0.08, -0.35, 0.17\}$ thus showing a good correlation of mean SM with the controls
483 especially antecedent rainfall. The additive and multiplicative bias for SMOS are $\delta =$
484 -0.003 and $\kappa = 0.15$ respectively, while the measurement error variance for SMAP
485 and SMOS are $\tau_{SMAP}^2 = 0.026$ and $\tau_{SMOS}^2 = 0.023$. To quantify the effect of covariates on
486 the spatio-temporal covariance of SM, we first transform the covariance to the original
487 scale. For a specified covariance between two points (from the covariance function in
488 equation 13) on the logit scale, we use the well-known Cholesky-Decomposition
489 method to simulate (50,000) pairs of values for these two points (Gong et al., 2013). We
490 then back-transform these values to the original scale and use the empirical covariance
491 of the pairs as an approximation of the covariance at the original scale.

492

493 For the non-stationary covariance function, since the covariance between any two
494 points depends on the lag-distance in space and time as well as the covariates (X_{cov}), the
495 effect of an individual covariate on the covariance is nontrivial. We thus quantify the
496 effect of a covariate by comparing the covariance for different lags (in space and time)
497 when the control is at the mean value (of the study domain) to when the control is at
498 extreme value (5th and 95th percentile) while keeping the other controls at their mean
499 values (Kathuria et al., 2019a; Reich et al., 2011). The resulting correlation plots are
500 given in Figure 6. We find that all four covariates affect the correlation in space with
501 higher values of rainfall, LAI, percent clay and lower values of elevation associated with
502 increase in spatial correlation. For the temporal correlation, we found only a slight effect
503 of the covariates on the correlation. Note, however, inclusion of other physical

504

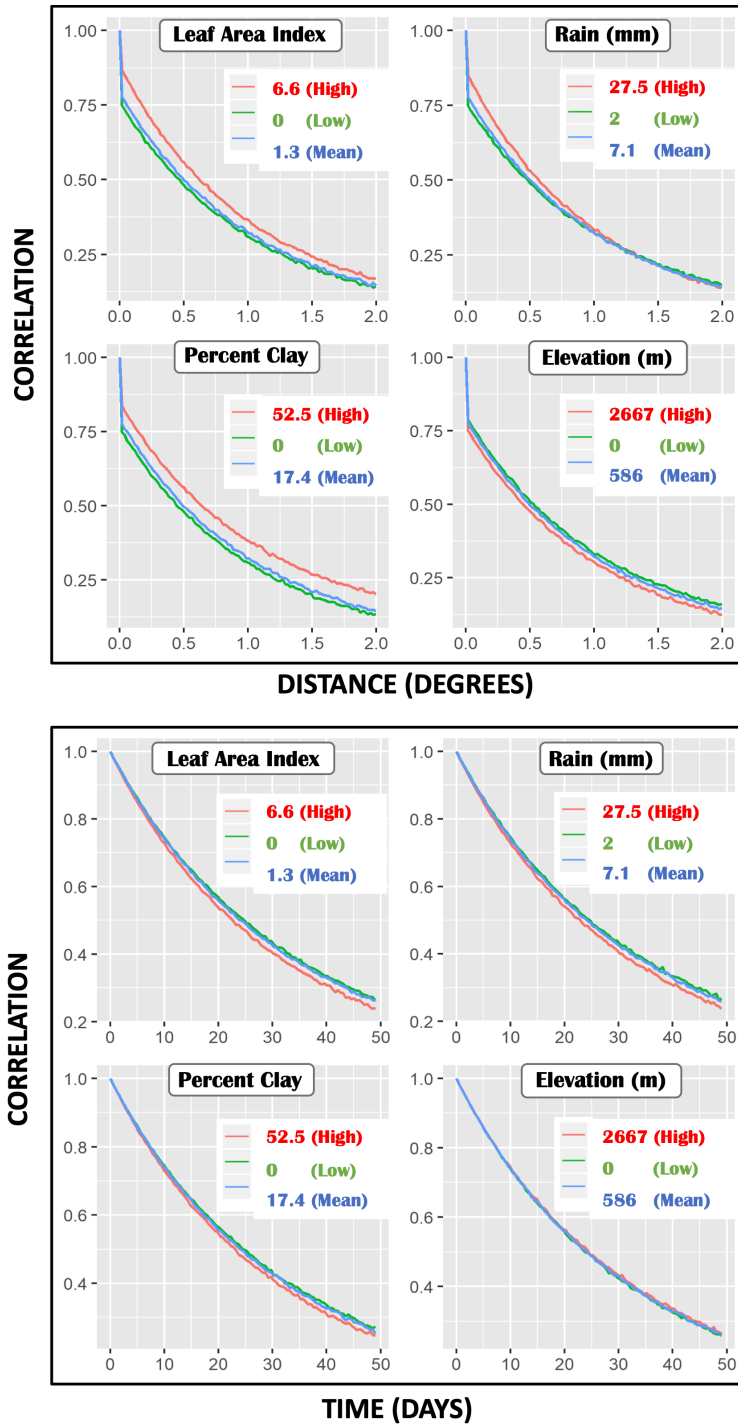


Figure 6. Spatial (top) and temporal (bottom) correlation plots when one of the physical covariates (Leaf Area Index, rainfall, clay and elevation) is changed from the mean value (of the study domain) to high (95th percentile) and low values (5th percentile). For each of the plots, the blue curve is the same representing the spatial and temporal correlation when all the covariates are at their mean values (LAI =1.3, Rain = 7.1 mm, Clay =17.4% and Elevation = 586 m) The red (green) curve refers to the correlation when one covariate is changed to a high (low) value keeping the other three covariates at the mean value.

506 covariates as well as analysis of a longer time-period might show the effect of certain
507 covariates on the temporal SM correlation.

508

509 Of course, individual plots in Figure 6 represent only three combinations of the physical
510 covariates. In reality, all the covariates exhibit considerable heterogeneity across
511 CONUS (Figure S6, SI) and act together to give vastly different correlation patterns. To
512 illustrate this effect, we choose 5 points (A-E, Figure 7) across CONUS under
513 contrasting covariate heterogeneity and look at the spatial correlation of these points
514 with surrounding points (~ 3 km apart) within an approximately $60\text{ km} \times 60\text{ km}$
515 region for July 06, 2017. We see that the correlation pattern differs significantly based on
516 the how the quartet of rainfall, LAI, clay and elevation vary in the surrounding region
517 of the respective points.

518

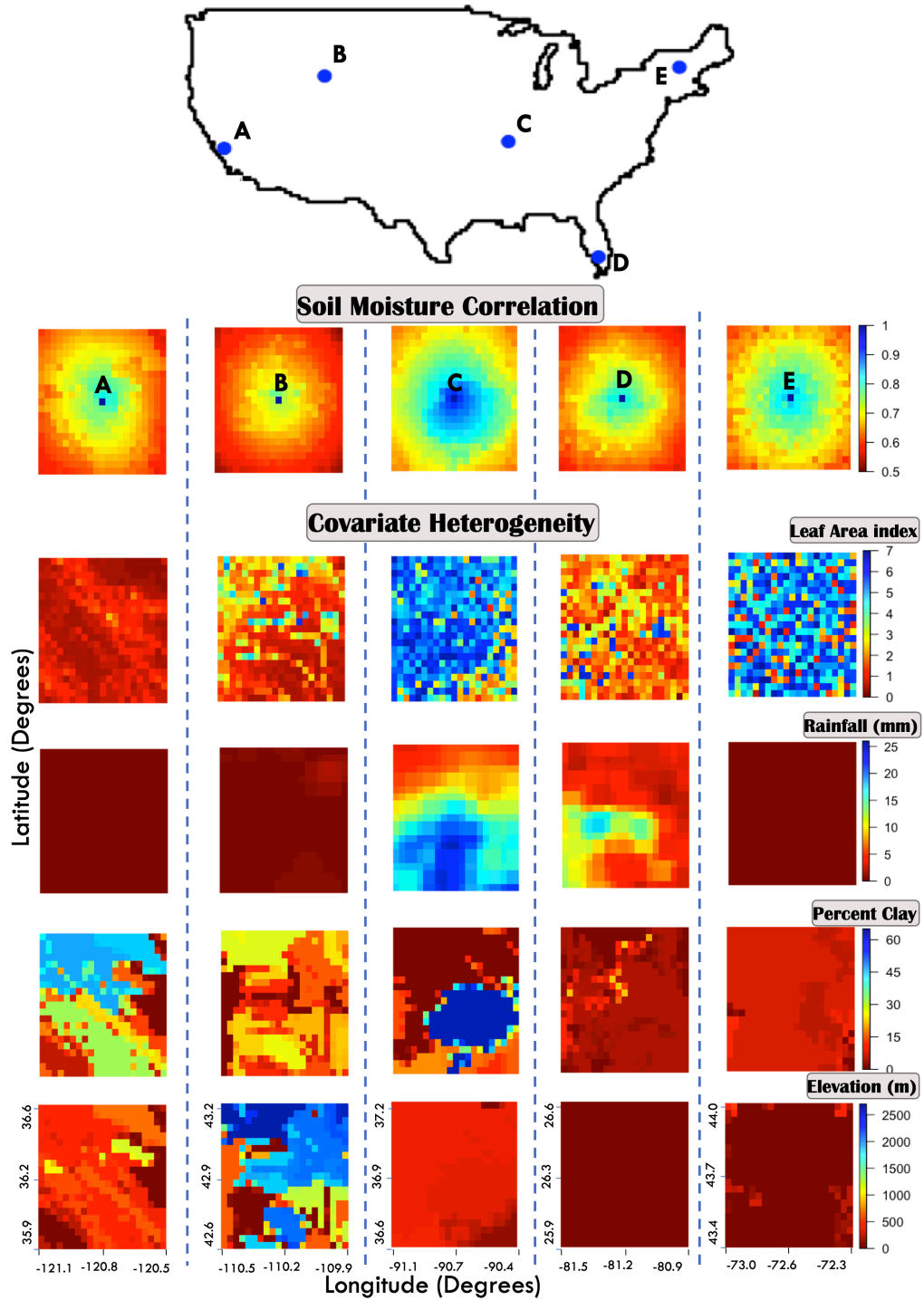
519 **4.2.3 Predictions at different Scales**

520 Once the parameters have been estimated, we compute multiscale SM predictions
521 (Appendix A1.2) across CONUS. As a final step, we back-transform the predictions i.e.,
522 $SM = \exp(SM') / (1 + \exp(SM'))$ to the original scale. We compare our SM predictions at
523 four support scales: point (USCRN and SCAN), 3 km (SMAP/Sentinel-1), 25 km
524 (SMOS) and 36 km (SMAP). We compute five-day SM forecasts from July 21-25, 2017 on
525 all four support scales.

526

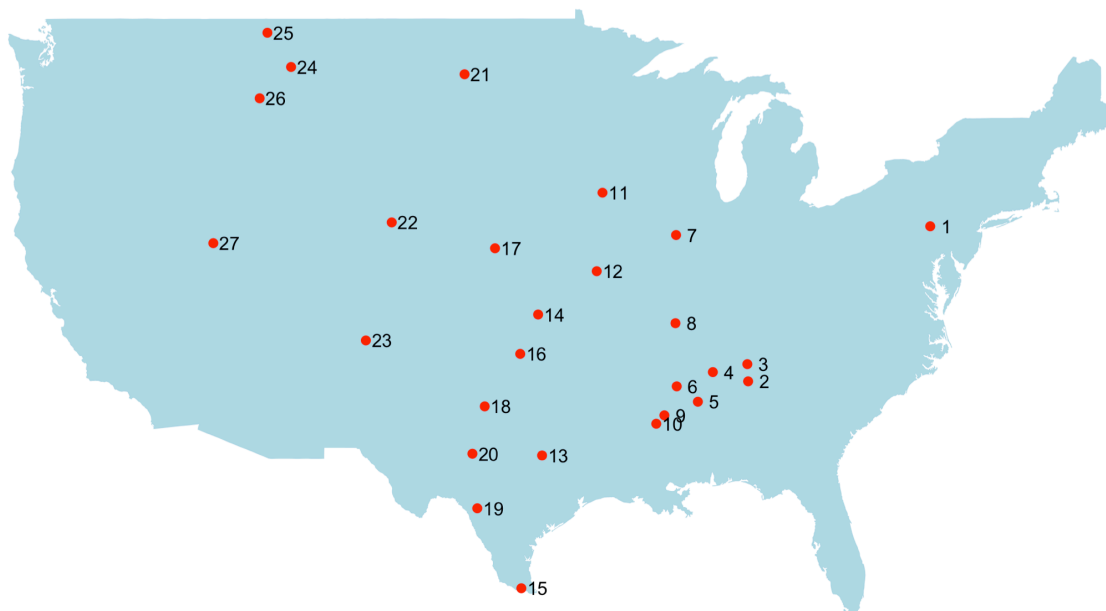
527 **4.2.3.1 USCRN and SCAN Scale**

528 As mentioned before, we randomly held out 27 USCRN and SCAN stations across
529 CONUS (Figure 8) as test data. Figure 9 depicts the SM for the “observed”



530

Figure 7. Spatial Correlation pattern of Soil moisture for five points (A-E) across Contiguous US for July 06, 2017. The correlation of the five points with their surrounding region varies considerably due to the covariate heterogeneity of the regions.

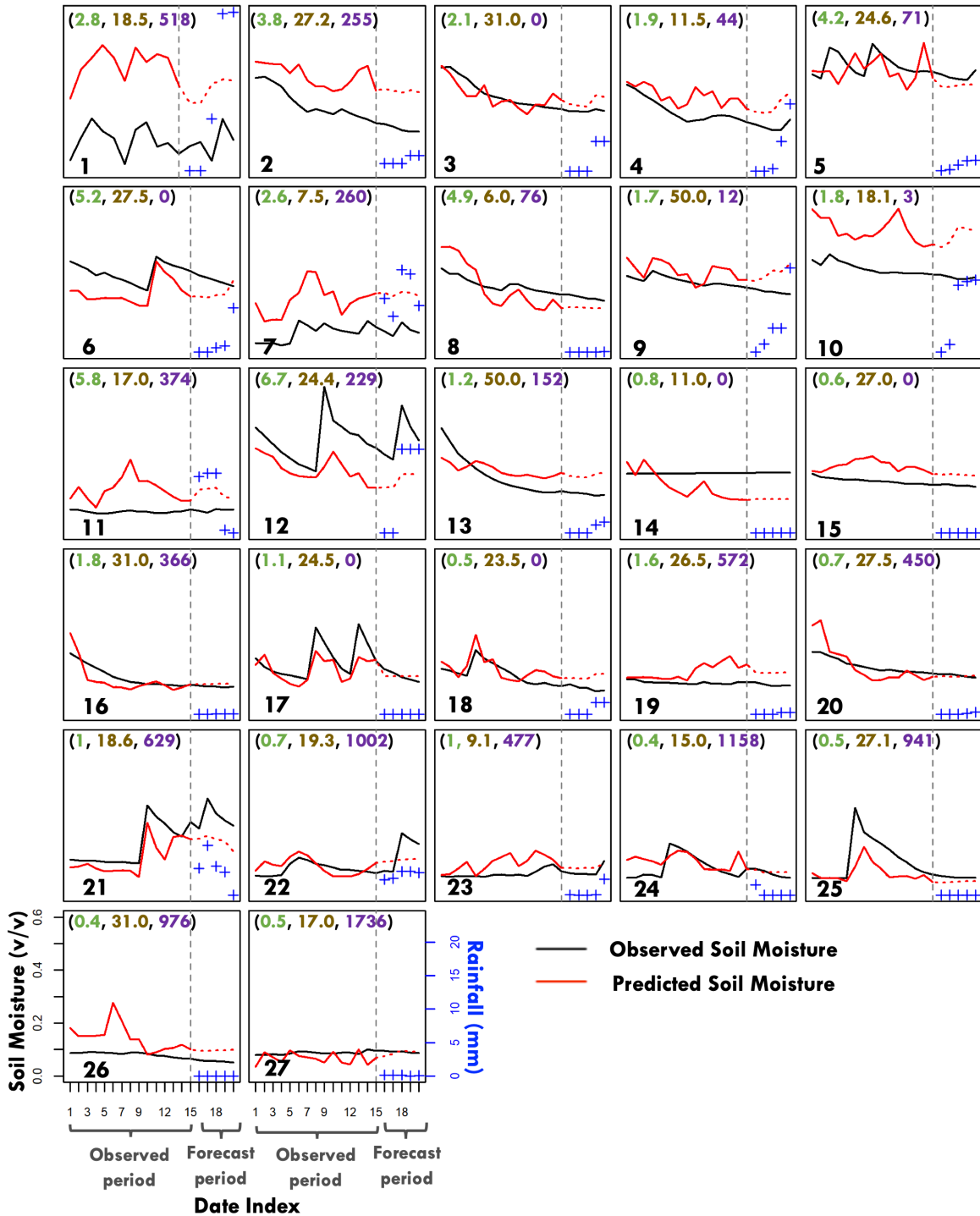


531

Figure 8. Location of the validation USCRN/SCAN stations across Contiguous US. We randomly hold out the 27 USCRN/SCAN stations to compare soil moisture predictions at the point scale across Contiguous US. The locations span different hydroclimates and surface heterogeneities.

532

533



534
535

Figure 9. Comparison of soil moisture predictions with the observed SCAN/USRN data for the “observed” (July 06-20, 2017) and “forecast” period (July 21-25, 2017). The covariate values of LAI (averaged during the forecast period), percent clay and elevation (m) are denoted by green, brown and purple colors respectively. The three-day mean antecedent rainfall is also given in blue during the forecast period to demonstrate its effect on SM forecasts.

536 (July 06-20, 2017) and “forecast” (July 21-25, 2017) period. For the observed period, the
537 correlation (R) and root mean squared error (RMSE) are 0.67 and 0.087 v/v respectively.
538 The slightly high value of the overall RMSE can be attributed to some point station data
539 where there is high bias between the predictions and observation (such as Site 1, 2, 7
540 and 10) and some stations where the observed SM does not change much during the 20-
541 day period (such as Site 14) possibly resulting from sensor malfunction. Though the SM
542 predictions during the observed period will be mainly influenced by SMAP and SMOS,
543 the predictions serve to fill in important gaps left by these platforms which observe SM
544 at a time interval of 3-7 days.

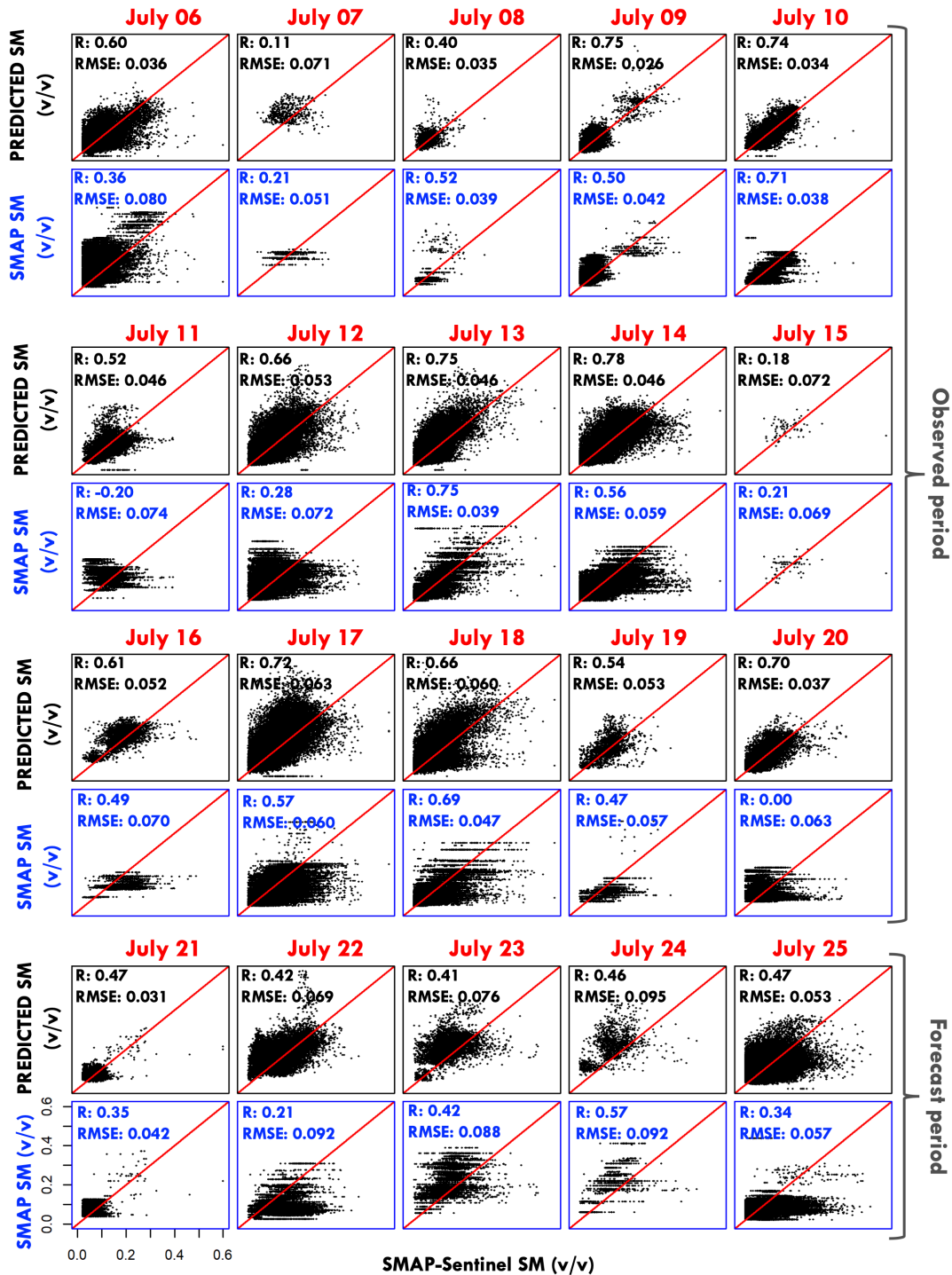
545

546 For the forecast period, R and RMSE of the sites are 0.57 and 0.086 v/v respectively. The
547 forecast period is especially important because it allows us to forecast five-day SM at
548 the point scale in the absence of any observed SM data. We plot the three-day mean
549 antecedent rainfall (from 4km PRISM data) during the forecast period to demonstrate
550 the wetting of SM in response to rainfall. The degree of wetting of SM in our predictions
551 varies not only with rainfall amount but also with the underlying land-surface
552 covariates. Overall, the forecasts for July 21-25, 2017 at point scale are satisfactory given
553 that we utilize only SMAP, SMOS and 116 point station (training) data across CONUS
554 during July 06-20, 2017. Better bias characterization driven by underlying surface
555 heterogeneity for both SMOS and SMAP can help to reduce the bias occurring at some
556 sites.

557

558 **4.2.3.2 SMAP/Sentinel-1 Scale**

559 The SMAP/Sentinel-1 L2 SM (Das et al., 2018) product uses concurrent 36 km SMAP T_b



560

Figure 10. Comparison of soil moisture predictions and SMAP soil moisture with the observed SMAP/Sentinel-1 soil moisture at 3 km scale. For the majority of the days, the predicted soil moisture using the fusion approach outperforms the original base SMAP product (even for the forecast period). The red line denotes the 1:1 line.

561 measurements and 3 km backscatter measurements from Sentinel-1 radars to give 3 km
562 SM in the overlapping regions of the two platforms. The Sentinel-1 radars have a much
563 narrower swath (~ 250 km) however, compared with the relatively wide swath (1,000
564 km) of SMAP which significantly reduces the spatial coverage of the SMAP/Sentinel-1
565 product. The average temporal revisit time of Sentinel-1 radars is 6 days and due to
566 different revisit times of SMAP and Sentinel-1 radars, the temporal resolution of the
567 SMAP/Sentinel-1 SM product varies from 6-12 days. Therefore, for any given day, the
568 coverage of the SMAP/Sentinel-1 product across CONUS is quite limited.

569

570 We compute SM predictions at 3 km (assuming the equidistant grid points \mathcal{G} to be 1 km
571 apart) for the observed SMAP/Sentinel-1 pixels during the 20-day period and compare
572 with the observed SMAP/Sentinel-1 product (Figure 10). We also compare the
573 SMAP/Sentinel-1 observations with the SMAP product from which it is derived. We
574 see that for the majority of the days the SM predictions agree well with the
575 SMAP/Sentinel-1 product outperforming the original SMAP product even for the
576 forecast period. This shows that fusing SMAP SM with SMOS (and USCRN-SCAN data)
577 and accounting for the effects of physical covariates on SM distribution results in better
578 predictive accuracy at 3 km support scale than just using the SMAP SM. Since the
579 spatio-temporal coverage of SMAP/Sentinel-1 is extremely limited, predictions using
580 the data fusion scheme are useful as they help predict SM across the entire CONUS at a
581 daily scale.

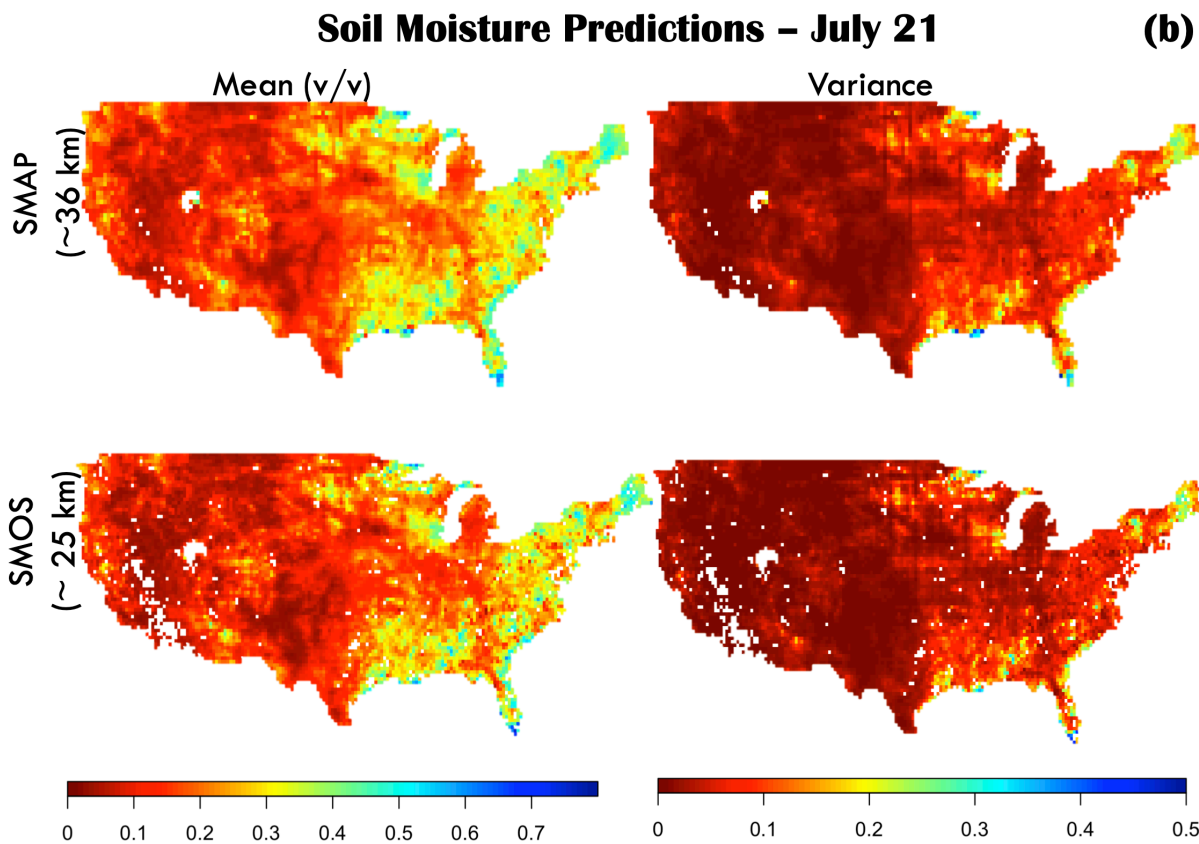
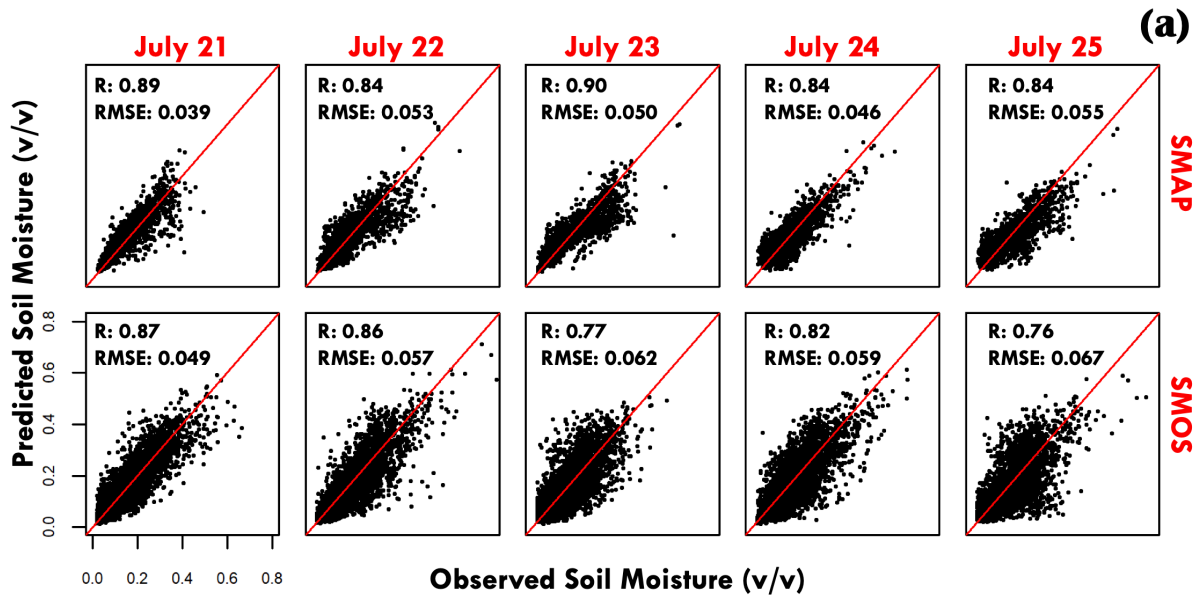
582

583 **4.2.3.3 SMAP and SMOS Scale**

584 Since we use all of SMAP and SMOS data for the “observed” period (July 06-20, 2017)
585 for estimating our parameters, we compare SM predictions with observed SMOS and
586 SMAP data for the forecast period (Figure 11 (a)). We make predictions assuming an
587 equidistant numerical grid spaced approximately 9 km apart and remove pixels which
588 have less than 7 grid points lying inside the pixels. We find that the predictions
589 satisfactorily agree with the observed SM with RMSE ranging from 0.039 v/v to 0.055
590 v/v for SMAP, and 0.049 v/v to 0.067 v/v for SMOS while R ranging from 0.84 to 0.90
591 for SMAP, and 0.76 to 0.87 for SMOS. As an illustration, the mean SM predictions as
592 well as the prediction variance for July 21, 2017 are given in Figure 11 (b). It should be
593 noted that since the multiscale predictions are derived from both SMOS and SMAP,
594 their accuracy is affected by how well the two platforms agree with each other. To get a
595 rough estimate of this, we bilinearly interpolated the SMOS pixels which overlap with
596 the SMAP pixels for July 21-25, 2017 and found an RMSE of 0.051 v/v to 0.076 v/v
597 while R varied from 0.74 to 0.86.

598

599 The proposed data fusion scheme thus shows good potential for improving SM
600 predictions across scales. Future research efforts should focus on applying the
601 algorithm for bigger time periods and across different seasons using high performance
602 computing systems. Improved formulations of the mean, bias and covariance functions
603 as well as the inclusion of other physical covariates should be explored. The accuracy of
604 the data fusion scheme at multiple scales can be improved by fusing SM estimates from
605 other platforms such as the Cyclone Global Navigation Satellite System (CYGNSS) and
606 the highly anticipated NASA-ISRO Synthetic Aperture Radar (NISAR) mission. The
607 data fusion allows seamless integration of any number of platforms at varied scales;
608 appropriate parametrization of the bias and error for individual platforms, however, is



609

Figure 11. (a) Comparison of soil moisture predictions and SMAP and SMOS observed soil moisture for July 21-25, 2017. The red line denotes the 1:1 line. (b) Soil moisture predictions across Contiguous US along with the prediction variance. Predictions are unavailable for certain regions due to absence of covariate data.

610 necessary. As mentioned earlier, the proposed algorithm is general and can be
611 potentially used to fuse other spatio-temporally correlated environmental variables
612 which have measurements available from multiple platforms.

613 **5 Conclusions**

614 In this work, we propose a geostatistical framework called *Vecchia-multiscale* for fusing
615 multiscale big data. Using simulated data, we found that certain orderings work better
616 in approximating the exact likelihood at a fraction of the computational cost. We then
617 apply *Vecchia-multiscale* to fuse real SM datasets and compute multiscale SM predictions
618 and forecast five-day SM across scales.

619

620 As the volume of environmental data are expected to dramatically increase in the
621 future, further research into finding better orderings becomes critical. We chose our
622 orderings based only on space and time; future work will focus on proposing
623 physically-based orderings where, in addition to the mean and covariance, the ordering
624 will also be covariate-driven. We applied *Vecchia-multiscale* to simulated data and real
625 SM observations; further application to diverse (spatio-temporally correlated)
626 environmental variables will vet the widespread utility of the algorithm. An advantage
627 of the proposed approach is that it is not a “black-box” and its components can be
628 readily modified based on the underlying physical variable and expert-knowledge.
629 Note that this algorithm can only be applied under a Gaussian Process assumption. In
630 cases where such an assumption is untenable, recent research indicates that the
631 approximation can be further extended using Generalized Gaussian Processes (Zilber &
632 Katzfuss, 2019).

633

634 We live in an exciting era where a deluge of environmental data presents an
635 unprecedented opportunity for uncovering hidden patterns existing in nature and
636 ultimately achieving the elusive mass and energy balance in Earth-System processes.
637 Data-fusion algorithms harnessing the combined utility of RS and insitu data are critical
638 to advance our understanding of global environmental processes at multiple scales and
639 make data-driven predictions. Moreover, since the breakthrough in numerical modeling
640 occurred when satellite data were assimilated in physical models, fusing multi-platform
641 satellite data can enhance the utility of existing physical models and help take the next
642 leap forward in understanding and predicting environmental processes.

643 **Acknowledgments**

644 We acknowledge the funding support from NASA grants NNX16AQ58G and
645 80NSSC20K1807, and Texas A&M University. Katzfuss was partially supported by
646 National Science Foundation (NSF) Grants DMS-1654083 and DMS-1953005. Portions of
647 this research were conducted with the advanced computing resources provided by
648 Texas A&M High Performance Research Computing. The data used in this study can be
649 accessed from the links provided below: <http://bec.icm.csic.es>;
650 <https://nsidc.org/data/SPL3SMP/versions/6>; https://nsidc.org/data/SPL2SMAP_S;
651 <http://doi.org/10.5067/MODIS/MCD15A3H.006>; <https://prism.oregonstate.edu>;
652 <https://data.nal.usda.gov/dataset/gridded-soil-survey-geographic-database-gssurgo>;
653 <https://catalog.data.gov/dataset/united-states-climate-reference-network-uscrn->

654 [processed-data-from-the-version-2-uscrn-database;](https://www.wcc.nrcs.usda.gov/scan;)
 655 <https://www.wcc.nrcs.usda.gov/scan.>

656 Appendix

657 A1. Parameter estimation and prediction for *Vecchia-multiscale*

658 A1.1 Parameter estimation

$$659 \quad f(z(\mathcal{A})) = f(z(A_1)|\theta) \times \prod_{i=2}^n f(z(A_i)|\mathbf{z}(\mathbf{A}_{1:i-1}), \theta) \quad (\text{A1})$$

660 where $\mathbf{A}_{1:i-1} = \{A_1, A_2, \dots, A_{i-1}\}$. If $z(\mathcal{A}) \sim N(\mu_z, \Sigma_z)$, then it can be shown that the $(i, j)^{th}$
 661 element of Λ —the inverse of Cholesky factor of Σ ($\Lambda^T \Lambda = \Sigma^{-1}$)— can be written as

$$662 \quad \lambda_{ij} = -\frac{w_{ij}}{\sigma_{z_i|z_{1:i-1}}^2} \quad (\text{A2})$$

663 where w_{ij} equals $\Sigma_{1:i-1}^{-1} C(\mathbf{A}_{1:i-1}, A_i)$ for $j = 1, \dots, i-1$, equals -1 for $j = i$, and equals 0
 664 for $j > i$. Here $\Sigma_{1:i-1} = C(\mathbf{A}_{1:i-1}, \mathbf{A}_{1:i-1}) + \tau^2 I_{i-1}$ and $\sigma_{z_i|z_{1:i-1}}^2 = C(A_i, A_i) -$

665 $C(A_i, \mathbf{A}_{1:i-1}) \Sigma_{1:i-1}^{-1} C(\mathbf{A}_{1:i-1}, A_i)$. Here I_{i-1} represents the identity matrix of size $i-1$. We

666 write $C(\mathbf{A}_{1:i-1}, A_i)_j \approx (h_{A_j}^k)^T C(\mathcal{G}_{A_j}, \mathcal{G}_{A_i}) h_{A_i}^k$ and $C(\mathbf{A}_{1:i-1}, \mathbf{A}_{1:i-1})_{jk} \approx$

667 $(h_{A_j}^k)^T C(\mathcal{G}_{A_j}, \mathcal{G}_{A_k}) h_{A_k}^k$ for $j, k = 1, \dots, i-1$ where \mathcal{G}_{A_l} denotes the subset of the total grid

668 points \mathcal{G} lying inside the pixel A_l and $h_{A_l}^k$ is given by equation 7.

669

670 We replace $\mathbf{A}_{1:i-1}$ with its subset \mathbf{A}_{m_i} of maximum length m as defined in Section 3.2.

671 This approximation leads to a sparse $\hat{\Lambda}$ because now $w_{ij} = 0$ for $j = 1, \dots, i-1$ if $j \notin m_i$,

672 leading to fast computation and low storage for $m \ll n$.

675

676 If $\mu(A_i) = X(A_i)^T \beta$ where $X(A_i) = \{X^1(A_i), \dots, X^p(A_i)\}$ is a vector of covariates of length
 677 p for pixel A_i . Then $\mu_{A_i} = X_{A_i} \beta$ in equation 9 where X_{A_i} is the matrix of covariates
 678 associated with the points associated with y_{A_i} in equation 7. Then μ_z (equation 8) can be
 679 written as $\tilde{X} \tilde{\beta}$ where the i^{th} row of \tilde{X} is given as $\{h_{A_i}^k X_{A_i}^1, \dots, h_{A_i}^k X_{A_i}^p, \delta(A_i)\}$. The parameter
 680 vector $\tilde{\beta}$ can be profiled out by using the profile-likelihood:

$$681 \quad -2 \log(f(z(\mathcal{A})|\theta)) = -2 \log(\det(\hat{\Lambda})) + (\hat{\Lambda}(z - \tilde{X} \tilde{\beta}))^T \hat{\Lambda}(z - \tilde{X} \tilde{\beta}) + n \log(2\pi) \quad (\text{A3})$$

682

683 The maximum likelihood estimate for $\tilde{\beta}$ is given as (Guinness, 2018; Stein et al., 2004):

$$684 \quad \tilde{\beta}_{MLE} = [(\hat{\Lambda} \tilde{X})^T (\hat{\Lambda} \tilde{X})]^{-1} (\hat{\Lambda} \tilde{X})^T (\hat{\Lambda} z) \quad (\text{A4})$$

685

686 **A1.2 Prediction Algorithm**

687 We follow the prediction algorithm from Guinness (2018). Let \mathcal{A}^{pred} denote a vector of
 688 length n^{pred} comprising pixels where we want to make predictions y^{pred} . Form
 689 the vector $\mathcal{A}^{comp} = (\mathcal{A}, \mathcal{A}^{pred})$ of length $n + n^{pred} = n^{comp}$. The corresponding
 690 observation-prediction vector is $y^{comp} = (z, y^{pred})$. Let the covariance matrix of y^{comp}
 691 be Σ^{comp} . Writing $\Sigma^{comp}(\Lambda^{comp})$ as a 2×2 block matrix $\{\Sigma_{ij}^{comp}\}_{i,j=1,2}$ ($\{\Lambda_{ij}^{comp}\}_{i,j=1,2}$) and
 692 using standard rules of multivariate normality:

$$693 \quad E[y^{pred}|z] = X^{pred} \beta + \Sigma_{21}^{comp} (\Sigma_{11}^{comp})^{-1} (z - \tilde{X} \tilde{\beta})$$

$$694 \quad = -(\Lambda_{22}^{comp})^{-1} \Lambda_{21}^{comp} z \approx -(\hat{\Lambda}_{22}^{comp})^{-1} \hat{\Lambda}_{21}^{comp} (z - \tilde{X} \tilde{\beta}), \quad (\text{A5})$$

695 where $\hat{\Lambda}^{comp}$ is the sparse approximation of Λ^{comp} calculated following A1.1.

696

697 To find the prediction variance $Var(y^{pred}|z)$, we first simulate uncorrelated standard698 normals of length n^{comp} ; $w^* \sim \mathcal{N}(0, I_{n^{comp}})$ where $I_{n^{comp}}$ is the identity matrix of size699 n^{comp} . We then simulate $y^{comp*} = \{z^*, y^{pred*}\} = (\hat{\Lambda}^{comp})^{-1}w$ which is computationally700 fast since $\hat{\Lambda}^{comp}$ is a sparse triangular matrix. Then, $-\hat{\Lambda}_{22}^{-1}\hat{\Lambda}_{21}(z - z^*) + y^{pred*}$ 701 approximately has a covariance matrix $\Sigma_{22}^{comp} - \Sigma_{21}^{comp}(\Sigma_{11}^{comp})^{-1}\Sigma_{12}^{comp}$, which is equal to702 $Var(y^{pred}|z)$ based on the well-known properties of multivariate normality. We703 simulate $-\hat{\Lambda}_{22}^{-1}\hat{\Lambda}_{21}(z - z^*) + y^{pred*}$ five thousand times to approximate the prediction

704 variance.

705 **References**

- 706 Akbar, R., Short Gianotti, D. J., Salvucci, G. D., & Entekhabi, D. (2019). Mapped Hydroclimatology of
 707 Evapotranspiration and Drainage Runoff Using SMAP Brightness Temperature Observations and
 708 Precipitation Information. *Water Resources Research*, 55(4), 3391–3413.
 709 <https://doi.org/10.1029/2018WR024459>
- 710 Barré, H. M. J. P., Duesmann, B., & Kerr, Y. H. (2008). SMOS: The mission and the system. *IEEE*
 711 *Transactions on Geoscience and Remote Sensing*, 46(3), 587–593.
 712 <https://doi.org/10.1109/TGRS.2008.916264>
- 713 Bauer, P., Thorpe, A., & Brunet, G. (2015). The quiet revolution of numerical weather prediction. *Nature*,
 714 525(7567), 47–55. <https://doi.org/10.1038/nature14956>
- 715 Camps-valls, G., Tuia, D., & Bruzzone, L. (2013). Advances in hyperspectral image classification. *IEEE*
 716 *Signal Processing Magazine*, January, 45–54.
- 717 Cecinati, F., Rico-Ramirez, M. A., Heuvelink, G. B. M., & Han, D. (2017). Representing radar rainfall
 718 uncertainty with ensembles based on a time-variant geostatistical error modelling approach. *Journal*
 719 *of Hydrology*, 548, 391–405. <https://doi.org/10.1016/j.jhydrol.2017.02.053>
- 720 Colliander, A., Jackson, T. J., Bindlish, R., Chan, S., Das, N., Kim, S. B., Cosh, M. H., Dunbar, R. S., Dang,
 721 L., Pashaian, L., Asanuma, J., Aida, K., Berg, A., Rowlandson, T., Bosch, D., Caldwell, T., Caylor, K.,
 722 Goodrich, D., al Jassar, H., ... Yueh, S. (2017). Validation of SMAP surface soil moisture products
 723 with core validation sites. *Remote Sensing of Environment*, 191, 215–231.
 724 <https://doi.org/10.1016/j.rse.2017.01.021>
- 725 Cosh, M. H., & Brutsaert, W. (1999). Aspects of soil moisture variability in the Washita '92 study region.
 726 *Journal of Geophysical Research: Atmospheres*, 104(D16), 19751–19757.
 727 <https://doi.org/https://doi.org/10.1029/1999JD900110>
- 728 Cressie, N. (1990). The origins of kriging. *Mathematical Geology*, 22(3), 239–252.
 729 <https://doi.org/10.1007/BF00889887>
- 730 Crow, W. T., Berg, A. A., Cosh, M. H., Loew, A., Mohanty, B. P., Panciera, R., de Rosnay, P., Ryu, D., &
 731 Walker, J. P. (2012). Upscaling sparse ground-based soil moisture observations for the validation of
 732 coarse-resolution satellite soil moisture products. *Reviews of Geophysics*, 50(2).
 733 <https://doi.org/https://doi.org/10.1029/2011RG000372>
- 734 Daly, C., Neilson, R. P., & Phillips, D. L. (1994). A statistical-topographic model for mapping
 735 climatological precipitation over mountainous terrain. *Journal of Applied Meteorology*.

- 736 [https://doi.org/10.1175/1520-0450\(1994\)033<0140:ASTMFM>2.0.CO;2](https://doi.org/10.1175/1520-0450(1994)033<0140:ASTMFM>2.0.CO;2)
 737 Das, N. N., Entekhabi, D., Dunbar, R. S., Kim, S., Yueh, S., Colliander, A., O'Neill, P. E., & Jackson, T.
 738 (2018). SMAP/Sentinel-1 L2 radiometer/radar 30-second scene 3 km EASE-grid soil moisture,
 739 version 2. *NASA National Snow and Ice Data Center DAAC*.
- 740 Datta, A., Banerjee, S., Finley, A. O., & Gelfand, A. E. (2016). Hierarchical Nearest-Neighbor Gaussian
 741 Process Models for Large Geostatistical Datasets. *Journal of the American Statistical Association*.
 742 <https://doi.org/10.1080/01621459.2015.1044091>
- 743 Diamond, H. J., Karl, T. R., Palecki, M. A., Baker, C. B., Bell, J. E., Leeper, R. D., Easterling, D. R.,
 744 Lawrimore, J. H., Meyers, T. P., Helfert, M. R., Goodge, G., & Thorne, P. W. (2013). U.S. climate
 745 reference network after one decade of operations status and assessment. *Bulletin of the American*
 746 *Meteorological Society*, 94(4), 485–498. <https://doi.org/10.1175/BAMS-D-12-00170.1>
- 747 Entekhabi, D., Njoku, E. G., O'Neill, P. E., Kellogg, K. H., Crow, W. T., Edelstein, W. N., Entin, J. K.,
 748 Goodman, S. D., Jackson, T. J., Johnson, J., Kimball, J., Piepmeier, J. R., Koster, R. D., Martin, N.,
 749 McDonald, K. C., Moghaddam, M., Moran, S., Reichle, R., Shi, J. C., ... Zyl, J. Van. (2010). The Soil
 750 Moisture Active Passive (SMAP) Mission. *Proceedings of the IEEE*, 98(5), 704–716.
 751 <https://doi.org/10.1109/JPROC.2010.2043918>
- 752 Entin, J. K., Robock, A., Vinnikov, K. Y., Hollinger, S. E., Liu, S., & Namkhai, A. (2000). Temporal and
 753 spatial scales of observed soil moisture variations in the extratropics. *Journal of Geophysical Research:*
 754 *Atmospheres*, 105(D9), 11865–11877. <https://doi.org/https://doi.org/10.1029/2000JD900051>
- 755 Evensen, G. (1994). Sequential data assimilation with a nonlinear quasi-geostrophic model using Monte
 756 Carlo methods to forecast error statistics. *Journal of Geophysical Research*, 99(C5).
 757 <https://doi.org/10.1029/94jc00572>
- 758 Fan, X., Liu, Y., Gan, G., & Wu, G. (2020). SMAP underestimates soil moisture in vegetation-disturbed
 759 areas primarily as a result of biased surface temperature data. *Remote Sensing of Environment*,
 760 247(November 2019), 111914. <https://doi.org/10.1016/j.rse.2020.111914>
- 761 Fang, K., Shen, C., Kifer, D., & Yang, X. (2017). Prolongation of SMAP to Spatiotemporally Seamless
 762 Coverage of Continental U.S. Using a Deep Learning Neural Network. *Geophysical Research Letters*,
 763 44(21), 11,030–11,039. <https://doi.org/10.1002/2017GL075619>
- 764 Gaur, N., & Mohanty, B. P. (2013). Evolution of physical controls for soil moisture in humid and
 765 subhumid watersheds. *Water Resources Research*. <https://doi.org/10.1002/wrcr.20069>
- 766 Gaur, N., & Mohanty, B. P. (2016). Land-surface controls on near-surface soil moisture dynamics:
 767 Traversing remote sensing footprints. *Water Resources Research*.
 768 <https://doi.org/10.1002/2015WR018095>
- 769 Gelfand, A. E. (2001). On the change of support problem for spatio-temporal data. *Biostatistics*, 2(1), 31–45.
 770 <https://doi.org/10.1093/biostatistics/2.1.31>
- 771 Gelfand, Alan E., Diggle, P. J., Fuentes, M., & Guttorp, P. (2010). *Handbook of Spatial Statistics*. CRC Press.
- 772 Ghil, M., & Malanotte-Rizzoli, P. (1991). Data Assimilation in Meteorology and Oceanography. *Advances*
 773 *in Geophysics*. [https://doi.org/10.1016/S0065-2687\(08\)60442-2](https://doi.org/10.1016/S0065-2687(08)60442-2)
- 774 Giroto, M., De Lannoy, G. J. M., Reichle, R. H., Rodell, M., Draper, C., Bhanja, S. N., & Mukherjee, A.
 775 (2017). Benefits and pitfalls of GRACE data assimilation: A case study of terrestrial water storage
 776 depletion in India. *Geophysical Research Letters*, 44(9), 4107–4115.
 777 <https://doi.org/10.1002/2017GL072994>
- 778 Goovaerts, P., Avruskin, G., Meliker, J., Slotnick, M., Jacquez, G., & Nriagu, J. (2005). Geostatistical
 779 modeling of the spatial variability of arsenic in groundwater of southeast Michigan. *Water Resources*
 780 *Research*, 41(7), 1–19. <https://doi.org/10.1029/2004WR003705>
- 781 Guinness, J. (2018). Permutation and Grouping Methods for Sharpening Gaussian Process
 782 Approximations. *Technometrics*, 60(4), 415–429. <https://doi.org/10.1080/00401706.2018.1437476>
- 783 Hengl, T., De Jesus, J. M., Heuvelink, G. B. M., Gonzalez, M. R., Kilibarda, M., Blagotić, A., Shangguan,
 784 W., Wright, M. N., Geng, X., Bauer-Marschallinger, B., Guevara, M. A., Vargas, R., MacMillan, R. A.,
 785 Batjes, N. H., Leenaars, J. G. B., Ribeiro, E., Wheeler, I., Mantel, S., & Kempen, B. (2017).
 786 SoilGrids250m: Global gridded soil information based on machine learning. *PLoS ONE*.
 787 <https://doi.org/10.1371/journal.pone.0169748>
- 788 Hu, G., Jia, L., & Menenti, M. (2015). Comparison of MOD16 and LSA-SAF MSG evapotranspiration
 789 products over Europe for 2011. *Remote Sensing of Environment*, 156, 510–526.
 790 <https://doi.org/10.1016/j.rse.2014.10.017>
- 791 Joshi, C., & Mohanty, B. P. (2010). Physical controls of near-surface soil moisture across varying spatial
 792 scales in an agricultural landscape during SMEX02. *Water Resources Research*, 46(12), 1–21.
 793 <https://doi.org/10.1029/2010WR009152>

- 794 Joshi, C., Mohanty, B. P., Jacobs, J. M., & Ines, A. V. M. (2011). Spatiotemporal analyses of soil moisture
795 from point to footprint scale in two different hydroclimatic regions. *Water Resources Research*, 47(1).
796 <https://doi.org/https://doi.org/10.1029/2009WR009002>
- 797 Jung, M., Reichstein, M., Ciais, P., Seneviratne, S. I., Sheffield, J., Goulden, M. L., Bonan, G., Cescatti, A.,
798 Chen, J., De Jeu, R., Dolman, A. J., Eugster, W., Gerten, D., Gianelle, D., Gobron, N., Heinke, J.,
799 Kimball, J., Law, B. E., Montagnani, L., ... Zhang, K. (2010). Recent decline in the global land
800 evapotranspiration trend due to limited moisture supply. *Nature*, 467(7318), 951–954.
801 <https://doi.org/10.1038/nature09396>
- 802 Kathuria, D., Mohanty, B. P., & Katzfuss, M. (2019a). A Nonstationary Geostatistical Framework for Soil
803 Moisture Prediction in the Presence of Surface Heterogeneity. *Water Resources Research*, 55(1).
804 <https://doi.org/10.1029/2018WR023505>
- 805 Kathuria, D., Mohanty, B. P., & Katzfuss, M. (2019b). Multiscale Data Fusion for Surface Soil Moisture
806 Estimation: A Spatial Hierarchical Approach. *Water Resources Research*, 55(12).
807 <https://doi.org/10.1029/2018WR024581>
- 808 Katzfuss, M., & Guinness, J. (2017). A general framework for Vecchia approximations of Gaussian
809 processes. In *arXiv*. <https://doi.org/10.1214/19-sts755>
- 810 Katzfuss, M., Guinness, J., Gong, W., & Zilber, D. (2020). Vecchia Approximations of Gaussian-Process
811 Predictions. *Journal of Agricultural, Biological, and Environmental Statistics*.
812 <https://doi.org/10.1007/s13253-020-00401-7>
- 813 Kaufman, C. G., Schervish, M. J., & Nychka, D. W. (2008). Covariance tapering for likelihood-based
814 estimation in large spatial data sets. *Journal of the American Statistical Association*.
815 <https://doi.org/10.1198/016214508000000959>
- 816 Klees, R., Zapreeva, E. A., Winsemius, H. C., & Savenije, H. H. G. (2007). The bias in GRACE estimates of
817 continental water storage variations. *Hydrology and Earth System Sciences*, 11(4), 1227–1241.
818 <https://doi.org/10.5194/hess-11-1227-2007>
- 819 Koster, Randal D., Brocca, L., Crow, W. T., Burgin, M. S., & De Lannoy, G. J. M. (2016). Precipitation
820 estimation using L-band and C-band soil moisture retrievals. *Water Resources Research*.
821 <https://doi.org/10.1002/2016WR019024>
- 822 Koster, Randal D., Crow, W. T., Reichle, R. H., & Mahanama, S. P. (2018). Estimating Basin-Scale Water
823 Budgets With SMAP Soil Moisture Data. *Water Resources Research*, 54(7), 4228–4244.
824 <https://doi.org/10.1029/2018WR022669>
- 825 Koster, Randall D., Schubert, S. D., & Suarez, M. J. (2009). Analyzing the concurrence of meteorological
826 droughts and warm periods, with implications for the determination of evaporative regime. *Journal*
827 *of Climate*. <https://doi.org/10.1175/2008JCLI2718.1>
- 828 Krige, D. G. (1952). A Statistical Approach to Some Basic Mine Valuation Problems on the Witwatersrand.
829 *Journal of the Chemical, Metallurgical and Mining Society of South Africa*.
830 <https://doi.org/10.2307/3006914>
- 831 Lanfredi, M., Coppola, R., D'Emilio, M., Imbrenda, V., Macchiato, M., & Simoniello, T. (2015). A
832 geostatistics-assisted approach to the deterministic approximation of climate data. *Environmental*
833 *Modelling and Software*, 66, 69–77. <https://doi.org/10.1016/j.envsoft.2014.12.009>
- 834 Lark, R. M. (2012). Towards soil geostatistics. *Spatial Statistics*, 1, 92–99.
835 <https://doi.org/10.1016/j.spasta.2012.02.001>
- 836 Li, S., Yu, Y., Sun, D., Tarpley, D., Zhan, X., & Chiu, L. (2014). Evaluation of 10 year AQUA/MODIS land
837 surface temperature with SURFRAD observations. *International Journal of Remote Sensing*, 35(3), 830–
838 856. <https://doi.org/10.1080/01431161.2013.873149>
- 839 Lievens, H., Reichle, R. H., Liu, Q., De Lannoy, G. J. M., Dunbar, R. S., Kim, S. B., Das, N. N., Cosh, M.,
840 Walker, J. P., & Wagner, W. (2017). Joint Sentinel-1 and SMAP data assimilation to improve soil
841 moisture estimates. *Geophysical Research Letters*. <https://doi.org/10.1002/2017GL073904>
- 842 Mao, H., Kathuria, D., Duffield, N., & Mohanty, B. P. (2019). Gap Filling of High-Resolution Soil Moisture
843 for SMAP/Sentinel-1: A Two-Layer Machine Learning-Based Framework. *Water Resources Research*.
844 <https://doi.org/10.1029/2019WR024902>
- 845 Mohanty, B. P., Ankeny, M. D., Horton, R., & Kanwar, R. S. (1994). Spatial analysis of hydraulic
846 conductivity measured using disc infiltrometers. *Water Resources Research*, 30(9), 2489–2498.
847 <https://doi.org/https://doi.org/10.1029/94WR01052>
- 848 Mohanty, B. P., Famiglietti, J. S., & Skaggs, T. H. (2000). Evolution of soil moisture spatial structure in a
849 mixed vegetation pixel during the Southern Great Plains 1997 (SGP97) Hydrology Experiment.
850 *Water Resources Research*, 36(12), 3675–3686.
851 <https://doi.org/https://doi.org/10.1029/2000WR900258>

- 852 Mohanty, B. P., & Kanwar, R. S. (1994). Spatial variability of residual nitrate-nitrogen under two tillage
853 systems in central Iowa: A composite three-dimensional resistant and exploratory approach. *Water*
854 *Resources Research*, 30(2), 237–251. <https://doi.org/10.1029/93WR02922>
- 855 Mohanty, B. P., Kanwar, R. S., & Horton, R. (1991). A Robust-Resistant Approach to Interpret Spatial
856 Behavior of Saturated Hydraulic Conductivity of a Glacial Till Soil Under No-Tillage System. *Water*
857 *Resources Research*, 27(11), 2979–2992. <https://doi.org/10.1029/91WR01720>
- 858 Myneni, R., Knyazikhin, Y., Park, T. (2015). MCD15A3H MODIS/Terra+Aqua Leaf Area Index/FPAR 4-day
859 L4 Global 500m SIN Grid V006. NASA EOSDIS Land Processes DAAC.
- 860 Nychka, D., Bandyopadhyay, S., Hammerling, D., Lindgren, F., & Sain, S. (2015). A Multiresolution
861 Gaussian Process Model for the Analysis of Large Spatial Datasets. *Journal of Computational and*
862 *Graphical Statistics*. <https://doi.org/10.1080/10618600.2014.914946>
- 863 O'Neill, P. E., Njoku, E. G., Jackson, T. J., Chan, S., & Bindlish, R. (2018). SMAP Algorithm Theoretical
864 Basis Document: Level 2 & 3 Soil Moisture (Passive) Data Products. *Revision D*.
- 865 Pablos, M., Vall-llossera, M., Piles, M., Camps, A., Gonzalez-Haro, C., Turiel, A., Herbert, C. J., Chaparro,
866 D., & Portal, G. (2019). *Influence of Quality Filtering Approaches in BEC SMOS L3 Soil Moisture*
867 *Products*. <https://doi.org/10.1109/igarss.2019.8900273>
- 868 Reich, B. J., Eidsvik, J., Guindani, M., Nail, A. J., & Schmidt, A. M. (2011). A class of covariate-dependent
869 spatiotemporal covariance functions for the analysis of daily ozone concentration. *Annals of Applied*
870 *Statistics*. <https://doi.org/10.1214/11-AOAS482>
- 871 Reichle, R. H., & Koster, R. D. (2004). Bias reduction in short records of satellite soil moisture. *Geophysical*
872 *Research Letters*, 31(19), 2–5. <https://doi.org/10.1029/2004GL020938>
- 873 Reichle, Rolf H., McLaughlin, D. B., & Entekhabi, D. (2002). Hydrologic data assimilation with the
874 ensemble Kalman filter. *Monthly Weather Review*, 130(1), 103–114. [https://doi.org/10.1175/1520-0493\(2002\)130<0103:HDAWTE>2.0.CO;2](https://doi.org/10.1175/1520-0493(2002)130<0103:HDAWTE>2.0.CO;2)
- 875 Reichstein, M., Camps-Valls, G., Stevens, B., Jung, M., Denzler, J., Carvalhais, N., & Prabhat. (2019). Deep
876 learning and process understanding for data-driven Earth system science. *Nature*, 566(7743), 195–
877 204. <https://doi.org/10.1038/s41586-019-0912-1>
- 878 Risser, M. D., & Calder, C. A. (2015). Regression-based covariance functions for nonstationary spatial
879 modeling. *Environmetrics*. <https://doi.org/10.1002/env.2336>
- 880 Ryu, D., & Famiglietti, J. S. (2006). Multi-scale spatial correlation and scaling behavior of surface soil
881 moisture. *Geophysical Research Letters*, 33(8).
882 <https://doi.org/10.1029/2006GL025831>
- 883 Schaefer, G. L., Cosh, M. H., & Jackson, T. J. (2007). The USDA Natural Resources Conservation Service
884 Soil Climate Analysis Network (SCAN). *Journal of Atmospheric and Oceanic Technology*, 24(12), 2073–
885 2077. <https://doi.org/10.1175/2007JTECHA930.1>
- 886 Shen, C. (2018). A Transdisciplinary Review of Deep Learning Research and Its Relevance for Water
887 Resources Scientists. *Water Resources Research*, 54(11), 8558–8593.
888 <https://doi.org/10.1029/2018WR022643>
- 889 Shi, X., Gao, Z., Lausen, L., Wang, H., Yeung, D. Y., Wong, W. K., & Woo, W. C. (2017). Deep learning for
890 precipitation nowcasting: A benchmark and a new model. *Advances in Neural Information Processing*
891 *Systems*.
- 892 Soil Survey Staff. (2020). *Gridded Soil Survey Geographic (gSSURGO) Database for the Conterminous United*
893 *States*. United States Department of Agriculture, Natural Resources Conservation Service.
894 <https://gdg.sc.egov.usda.gov/>
- 895 Stein, M. L., Chi, Z., & Wely, L. J. (2004). Approximating likelihoods for large spatial data sets. *Journal of*
896 *the Royal Statistical Society. Series B: Statistical Methodology*. <https://doi.org/10.1046/j.1369-7412.2003.05512.x>
- 897 Sun, Y., & Stein, M. L. (2016). Statistically and Computationally Efficient Estimating Equations for Large
898 Spatial Datasets. *Journal of Computational and Graphical Statistics*.
899 <https://doi.org/10.1080/10618600.2014.975230>
- 900 Teuling, A. J., & Troch, P. A. (2005). Improved understanding of soil moisture variability dynamics.
901 *Geophysical Research Letters*, 32(5). <https://doi.org/10.1029/2004GL021935>
- 902 Vecchia, A. V. (1988). Estimation and Model Identification for Continuous Spatial Processes. *Journal of the*
903 *Royal Statistical Society: Series B (Methodological)*. <https://doi.org/10.1111/j.2517-6161.1988.tb01729.x>
- 904 Velpuri, N. M., Senay, G. B., Singh, R. K., Bohms, S., & Verdin, J. P. (2013). A comprehensive evaluation of
905 two MODIS evapotranspiration products over the conterminous United States: Using point and
906 gridded FLUXNET and water balance ET. *Remote Sensing of Environment*, 139, 35–49.
907 <https://doi.org/10.1016/j.rse.2013.07.013>

- 910 Vereecken, H., Huisman, J. A., Pachepsky, Y., Montzka, C., van der Kruk, J., Bogaen, H., Weihermüller,
 911 L., Herbst, M., Martinez, G., & Vanderborght, J. (2014). On the spatio-temporal dynamics of soil
 912 moisture at the field scale. *Journal of Hydrology*, 516, 76–96.
 913 <https://doi.org/https://doi.org/10.1016/j.jhydrol.2013.11.061>
- 914 Wang, B., Zou, X., & Zhu, J. (2000). Data assimilation and its applications. *Proceedings of the National*
 915 *Academy of Sciences of the United States of America*, 97(21), 11143–11144.
 916 <https://doi.org/10.1073/pnas.97.21.11143>
- 917 Westermann, S., Langer, M., & Boike, J. (2012). Systematic bias of average winter-time land surface
 918 temperatures inferred from MODIS at a site on Svalbard, Norway. *Remote Sensing of Environment*,
 919 118, 162–167. <https://doi.org/10.1016/j.rse.2011.10.025>
- 920 Wikle, C. K., Zammit-Mangion, A., & Cressie, N. (2019). *Spatio-Temporal Statistics with R*. CRC Press.
- 921 Xiang, Y., Gubian, S., Suomela, B., & Hoeng, J. (2013). Generalized simulated annealing for global
 922 optimization: The GenSA package. *R Journal*. <https://doi.org/10.32614/rj-2013-002>
- 923 Zhong, Z., & Carr, T. R. (2019). Geostatistical 3D geological model construction to estimate the capacity of
 924 commercial scale injection and storage of CO₂ in Jacksonburg-Stringtown oil field, West Virginia,
 925 USA. *International Journal of Greenhouse Gas Control*, 80(March 2018), 61–75.
 926 <https://doi.org/10.1016/j.ijggc.2018.10.011>
- 927 Zilber, D., & Katzfuss, M. (2019). *Vecchia-Laplace approximations of generalized Gaussian processes for big non-*
 928 *Gaussian spatial data*.
- 929